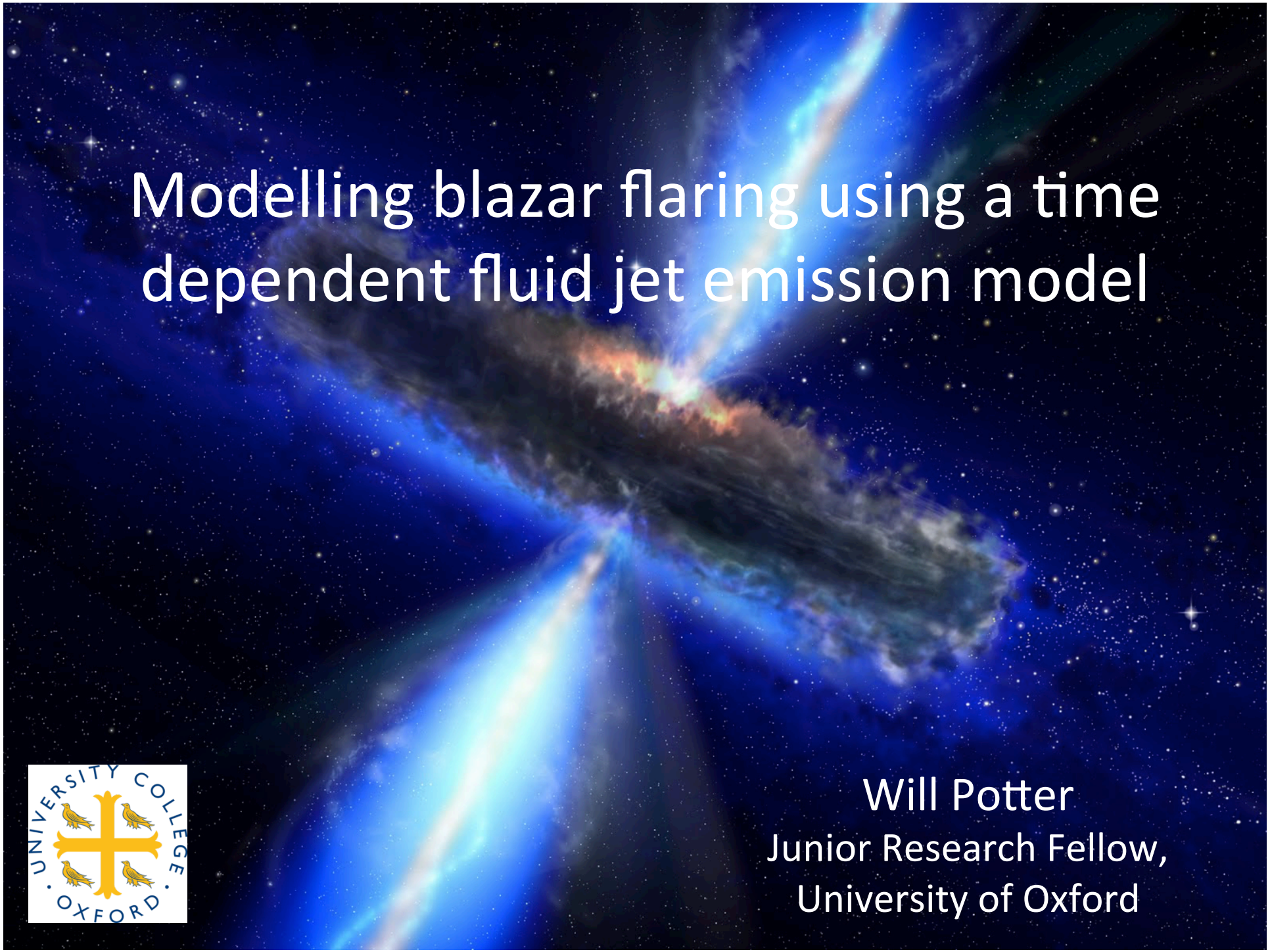

Modelling blazar flaring using a time dependent fluid jet emission model

Will Potter
Junior Research Fellow,
University of Oxford

Outline

- An extended relativistic fluid jet emission model based on observations of M87.
- Fitting radio observations to constrain the structure and dynamics of jets.
- Modelling time-dependent multi-frequency flares.
- Understanding radio lags and orphan flares.

Jet simulations

- General relativistic MHD simulations find jets which start magnetically dominated and parabolic in the accelerating region.
- Once the jets have accelerated and converted most of the magnetic energy into bulk kinetic energy the acceleration ceases to be efficient and the jets become ballistic and conical.

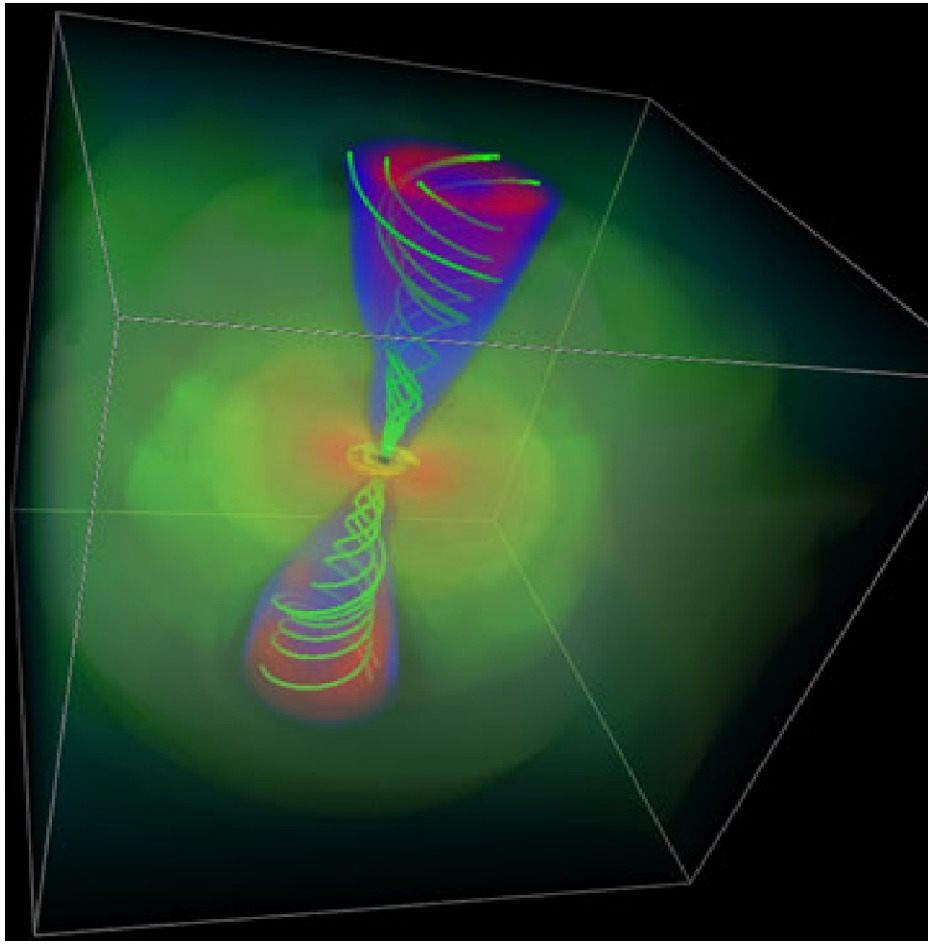

McKinney and Blandford 2009

Observations of M87

- VLBI observations of M87 show the jet starts parabolic and accelerating and this transitions to conical decelerating jet at ~10^5 r_s.

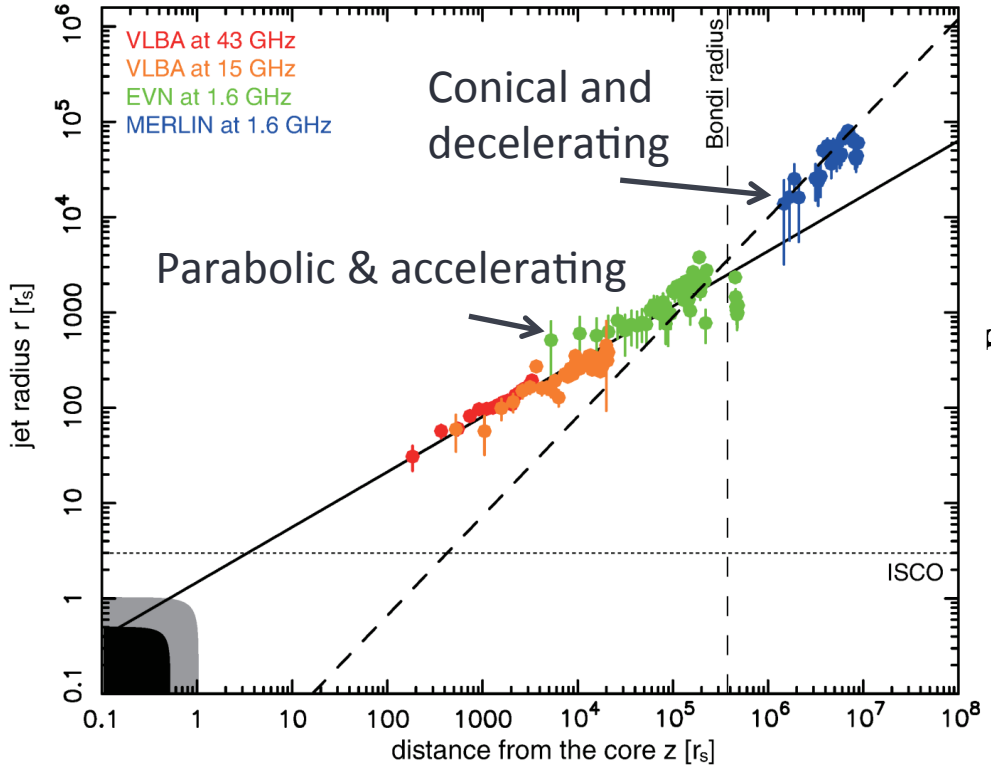

Asada and Nakamura 2012

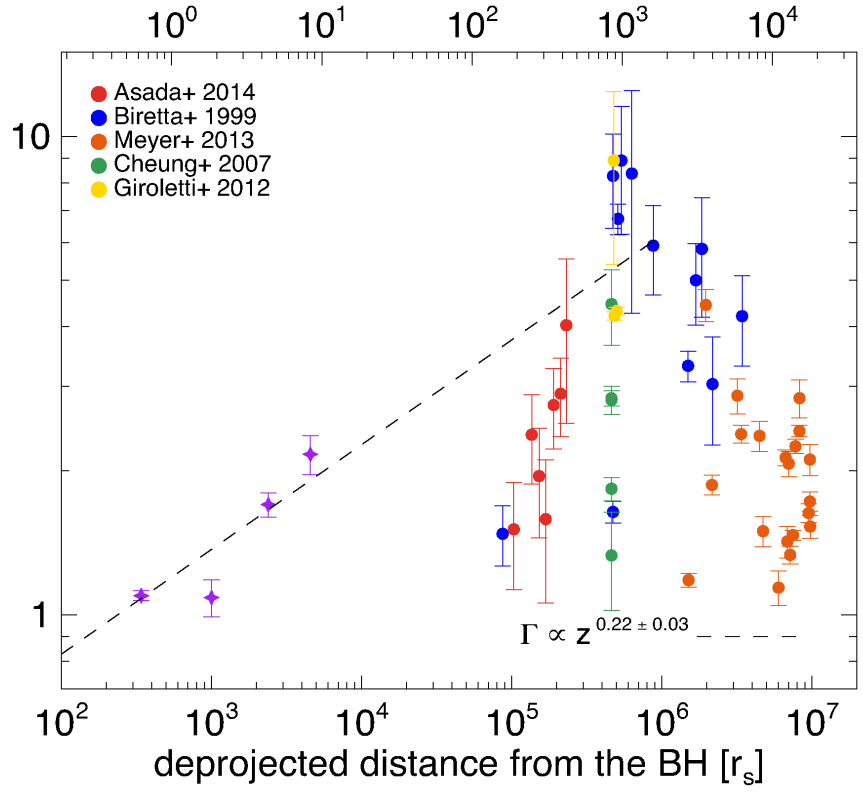

Hada et al. 2014

A realistic fluid model for jet emission

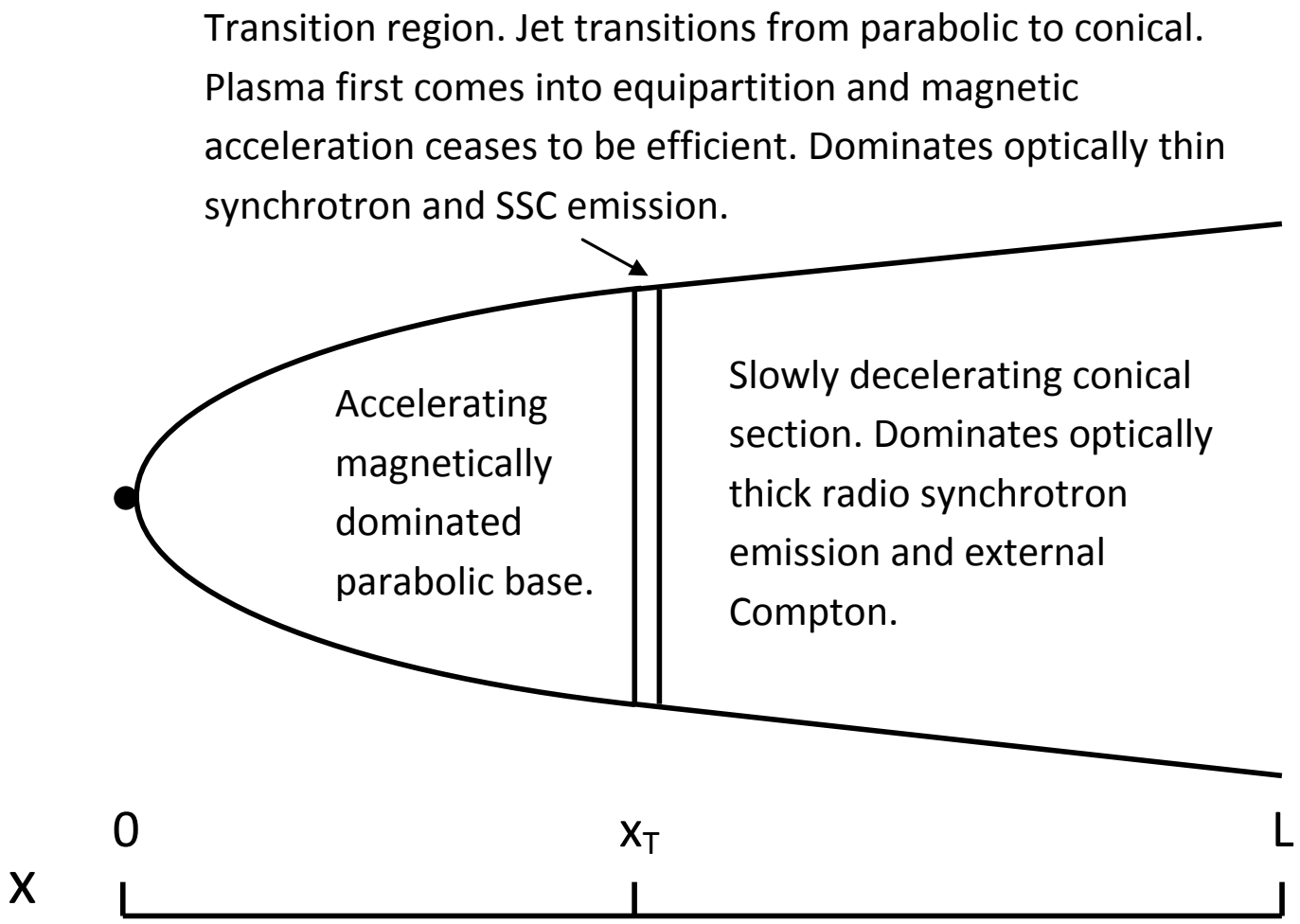

Potter and Cotter 2013a

A relativistic fluid jet emission model

- Relativistic energy-momentum and particle number flux are conserved along the fluid jet.
- The population of non-thermal electrons is evolved along the jet experiencing in situ acceleration and radiative losses.
- The jet structure is divided into thousands of cylindrical sections and the synchrotron and inverse-Compton emission calculated from each.
- A detailed treatment of the external photon sources from the accretion disc, BLR, dusty torus, NLR, starlight and CMB.
- The synchrotron and pair-production opacities are integrated through the jet to each section.

Fitting the quiescent model to spectra

- The first time a model fits to both radio and gamma-ray blazar observations simultaneously and with unprecedented accuracy.

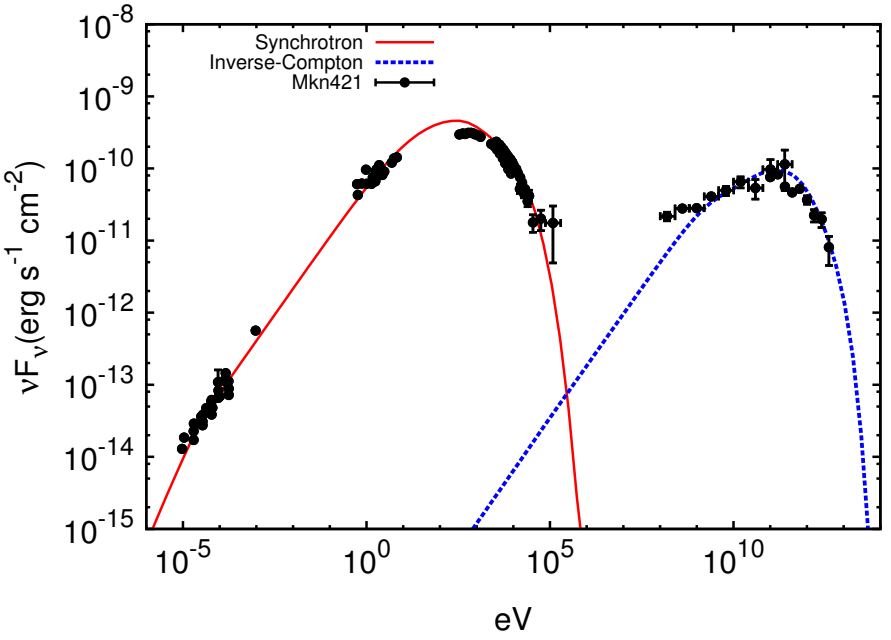

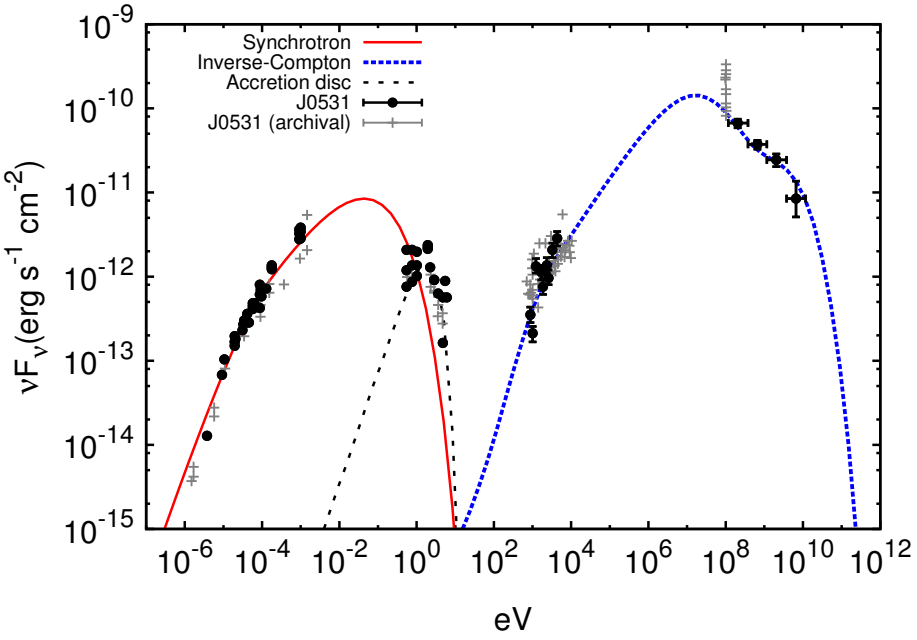

Potter and Cotter 2013b, 2013c and 2015

Fitting to 38 simultaneous multiwavelength Fermi blazars

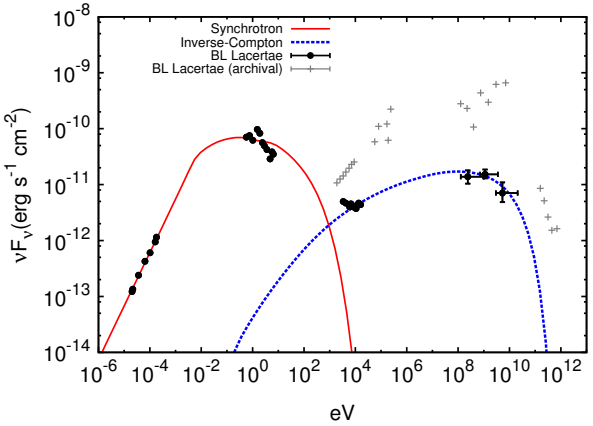

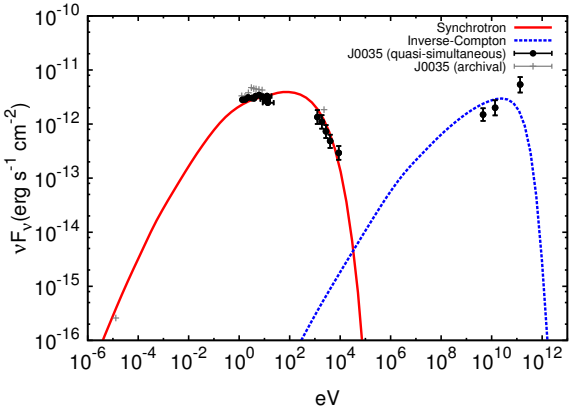

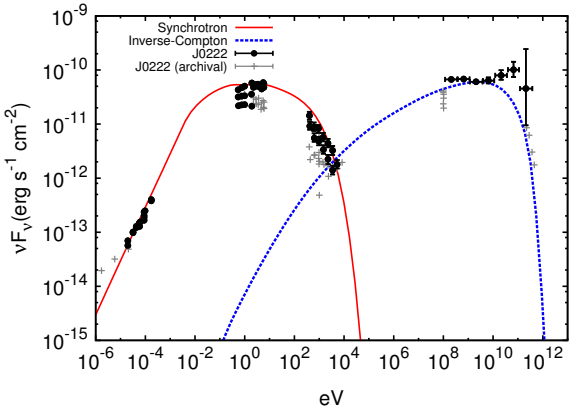

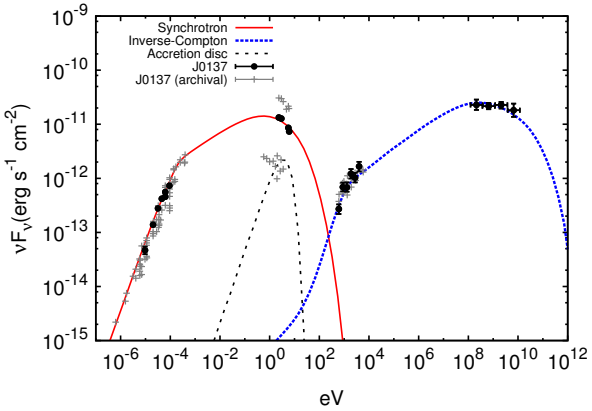

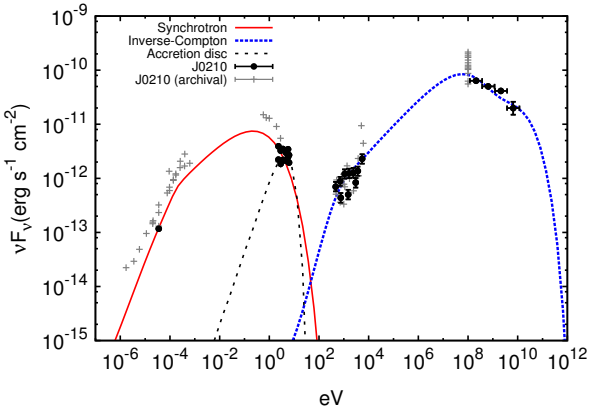

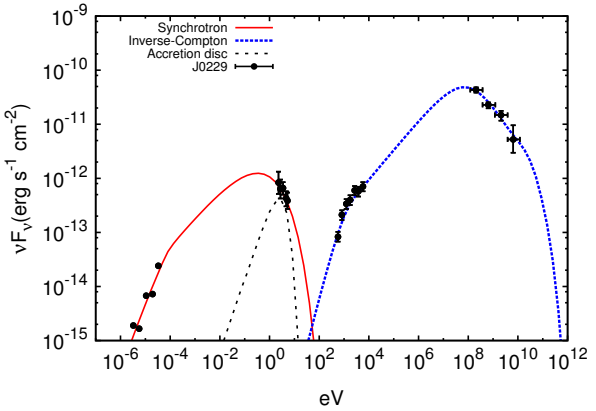

Potter and Cotter 2013b, 2013c and 2015

SED data from Abdo et al. 2009

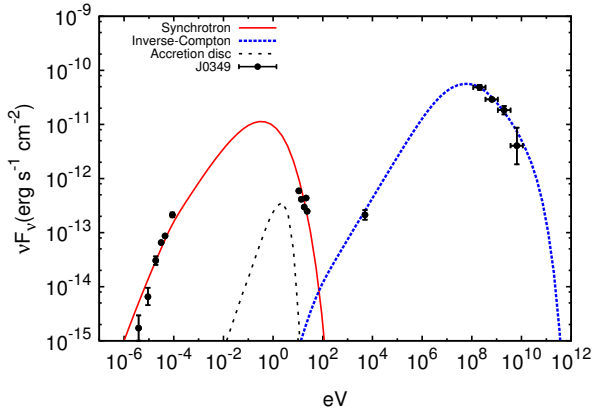
Synchrotron
Inverse-Compton
Accretion disc
J0349
vF_ν(erg s^{-1} cm^{-2})
eV

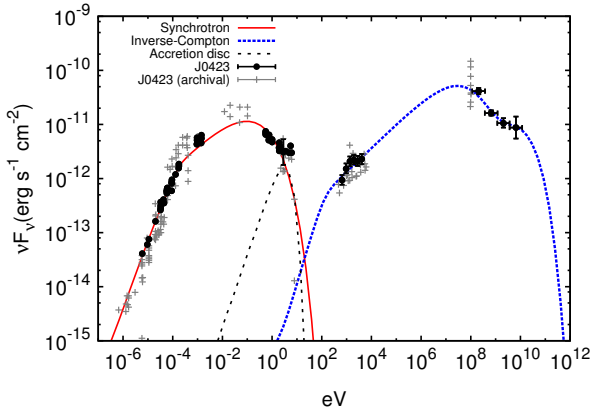
Synchrotron
Inverse-Compton
Accretion disc
J0423
J0423 (archival)
vF_ν(erg s^{-1} cm^{-2})
eV

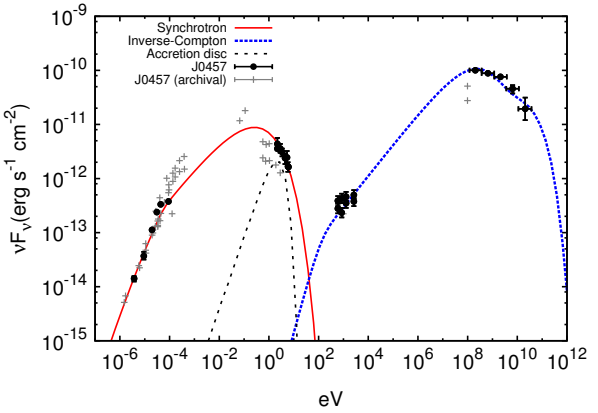
Synchrotron
Inverse-Compton
Accretion disc
J0457
J0457 (archival)
vF_ν(erg s^{-1} cm^{-2})
eV

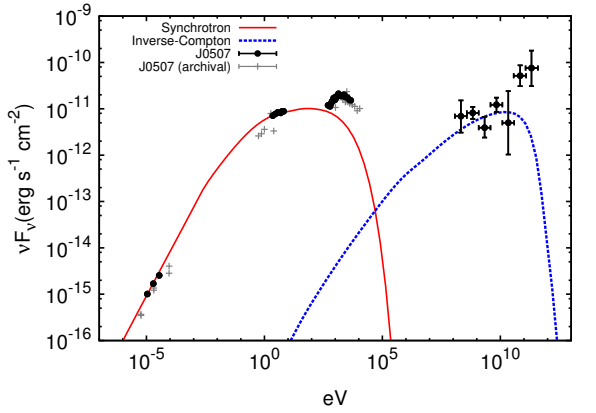
Synchrotron
Inverse-Compton
J0507
J0507 (archival)
vF_ν(erg s^{-1} cm^{-2})
eV

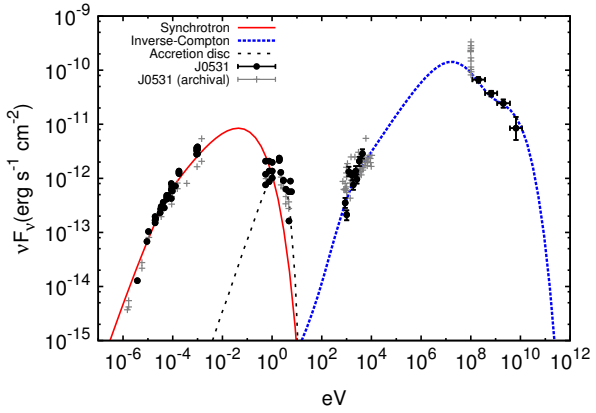
Synchrotron
Inverse-Compton
Accretion disc
J0531
J0531 (archival)
vF_ν(erg s^{-1} cm^{-2})
eV

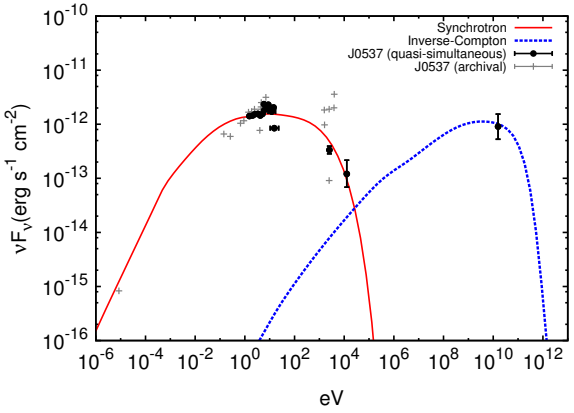
Synchrotron
Inverse-Compton
J0537 (quasi-simultaneous)
J0537 (archival)
vF_ν(erg s^{-1} cm^{-2})
eV

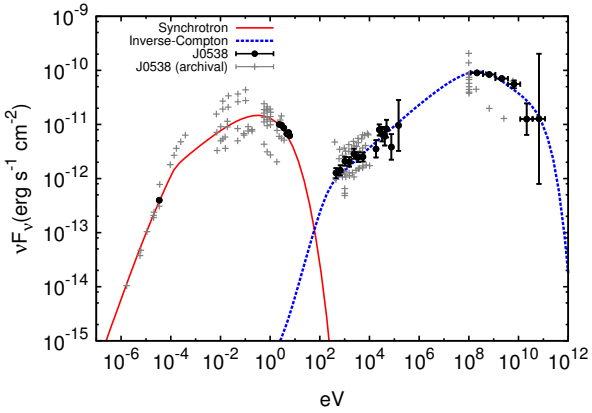
Synchrotron
Inverse-Compton
J0538
J0538 (archival)
νF_ν(erg s^{-1} cm^{-2})
eV

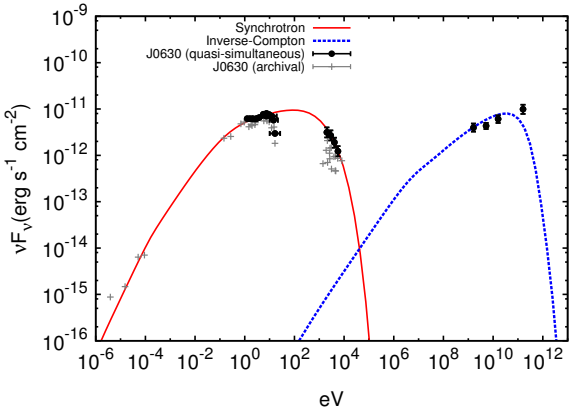
Synchrotron
Inverse-Compton
J0630 (quasi-simultaneous)
J0630 (archival)
νF_ν(erg s^{-1} cm^{-2})
eV

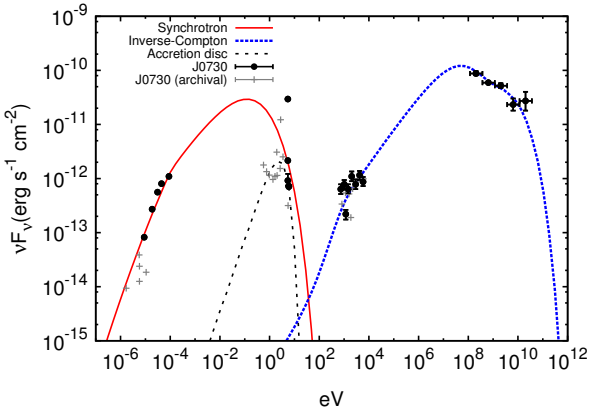
Synchrotron
Inverse-Compton
Accretion disc
J0730
J0730 (archival)
νF_ν(erg s^{-1} cm^{-2})
eV

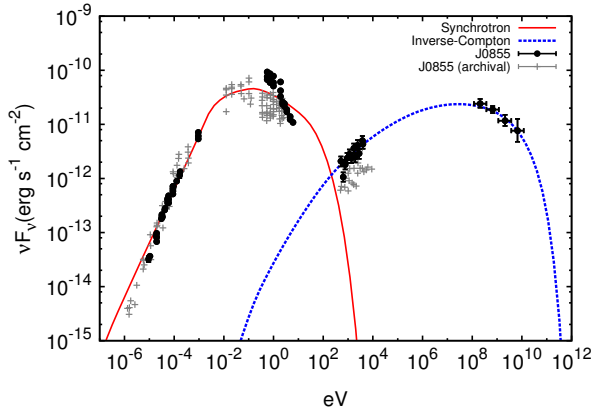
Synchrotron
Inverse-Compton
J0855
J0855 (archival)
νF_ν(erg s^{-1} cm^{-2})
eV

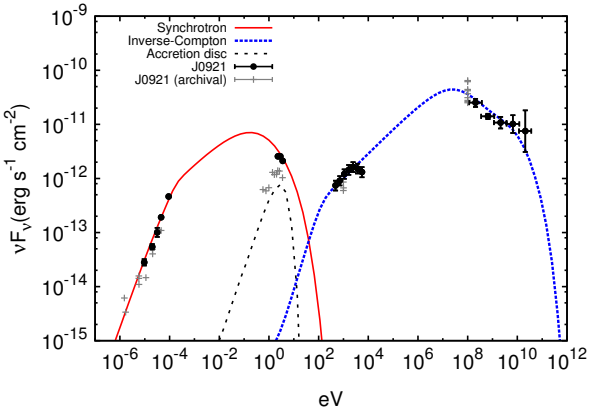
Synchrotron
Inverse-Compton
Accretion disc
J0921
J0921 (archival)
νF_ν(erg s^{-1} cm^{-2})
eV

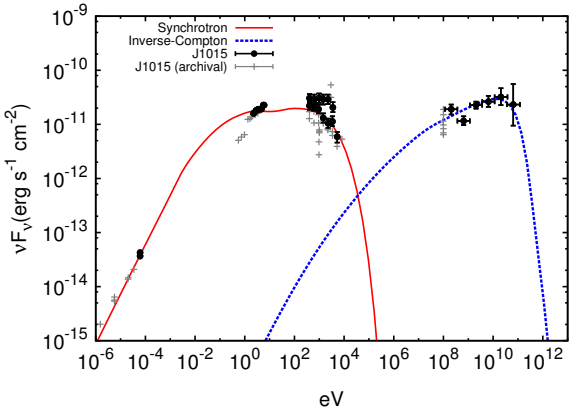
Synchrotron
Inverse-Compton
J1015
J1015 (archival)
νF_ν(erg s^{-1} cm^{-2})
eV

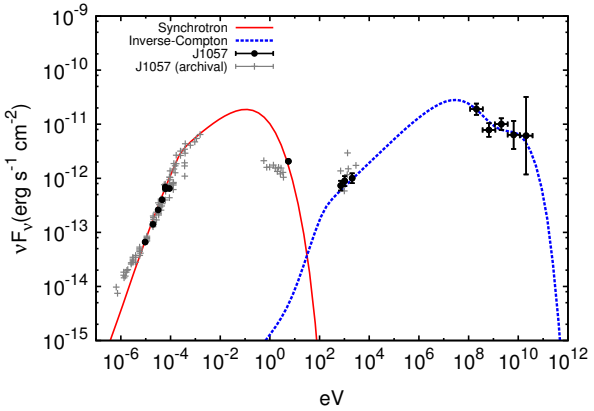
Synchrotron
Inverse-Compton
J1057
J1057 (archival)
vF$_\nu$(erg s^{-1} cm^{-2})
eV

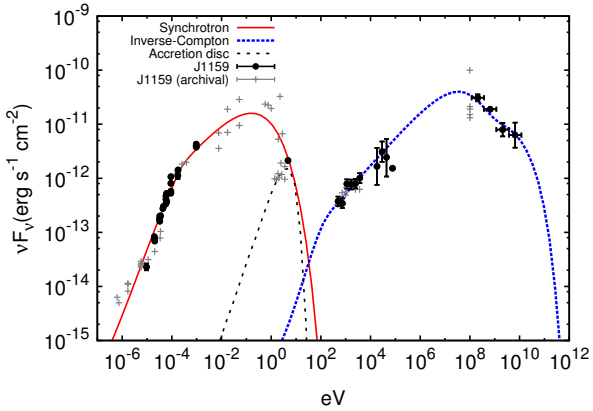
Synchrotron
Inverse-Compton
Accretion disc
J1159
J1159 (archival)
vF$_\nu$(erg s^{-1} cm^{-2})
eV

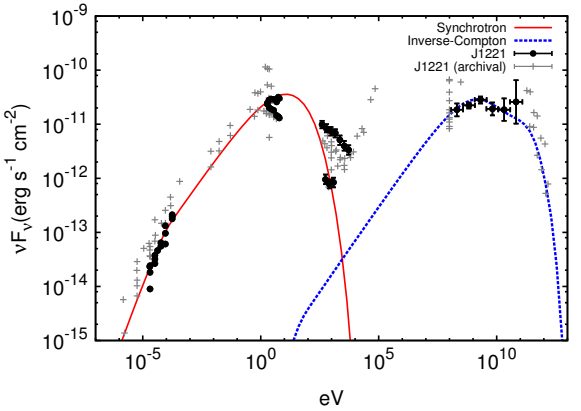
Synchrotron
Inverse-Compton
J1221
J1221 (archival)
vF$_\nu$(erg s^{-1} cm^{-2})
eV

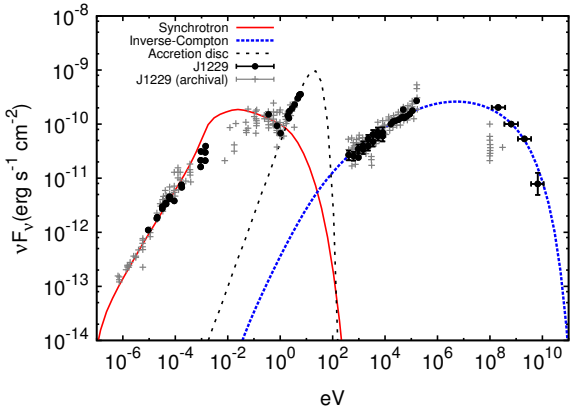
Synchrotron
Inverse-Compton
Accretion disc
J1229
J1229 (archival)
vF$_\nu$(erg s^{-1} cm^{-2})
eV

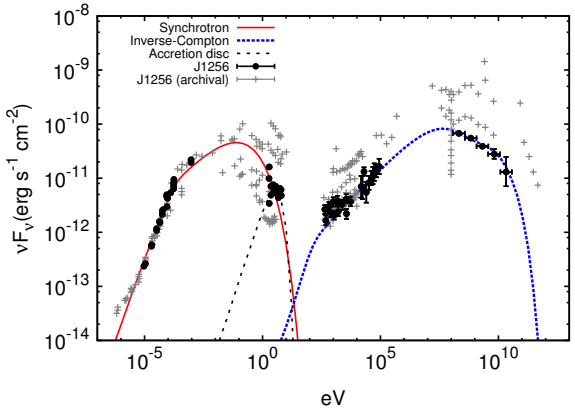
Synchrotron
Inverse-Compton
Accretion disc
J1256
J1256 (archival)
vF$_\nu$(erg s^{-1} cm^{-2})
eV

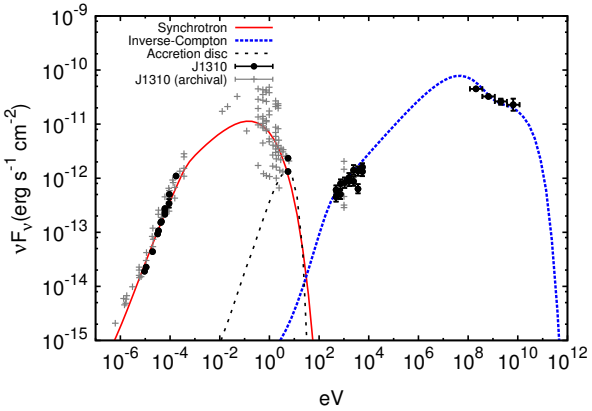
Synchrotron
Inverse-Compton
Accretion disc
J1310
J1310 (archival)
vF$_\nu$(erg s^{-1} cm^{-2})
eV

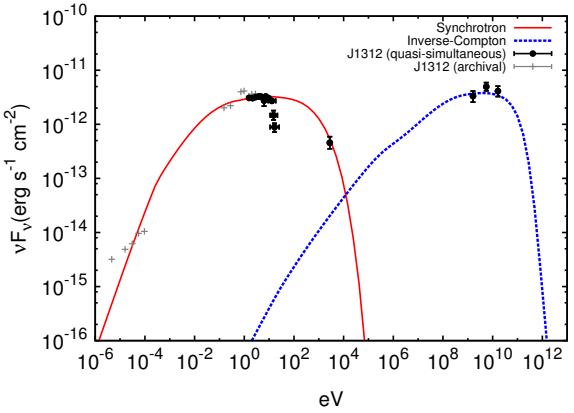
Synchrotron
Inverse-Compton
J1312 (quasi-simultaneous)
J1312 (archival)
vF$_\nu$(erg s^{-1} cm^{-2})
eV

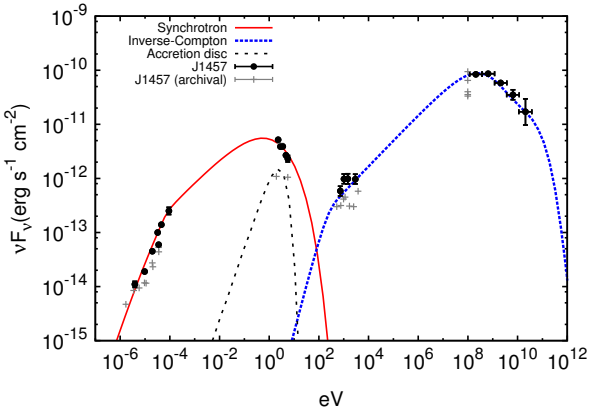
Synchrotron
Inverse-Compton
Accretion disc
J1457
J1457 (archival)
vF$_\nu$(erg s^{-1} cm^{-2})
eV

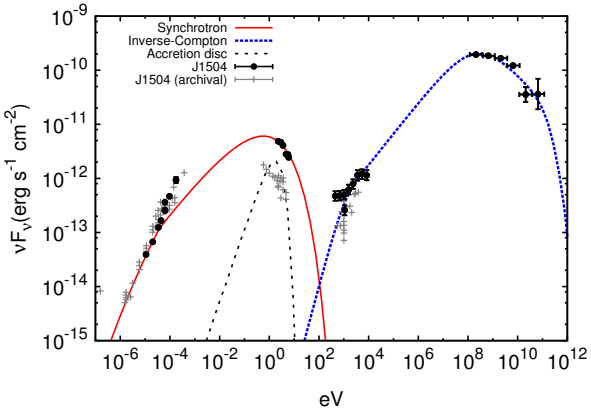
Synchrotron
Inverse-Compton
Accretion disc
J1504
J1504 (archival)
vF$_\nu$(erg s^{-1} cm^{-2})
eV

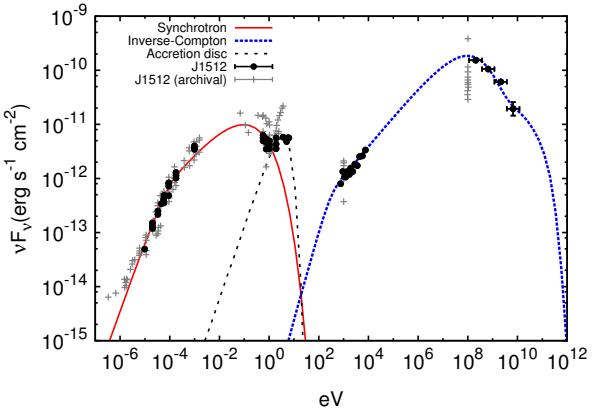
Synchrotron
Inverse-Compton
Accretion disc
J1512
J1512 (archival)
vF$_\nu$(erg s^{-1} cm^{-2})
eV

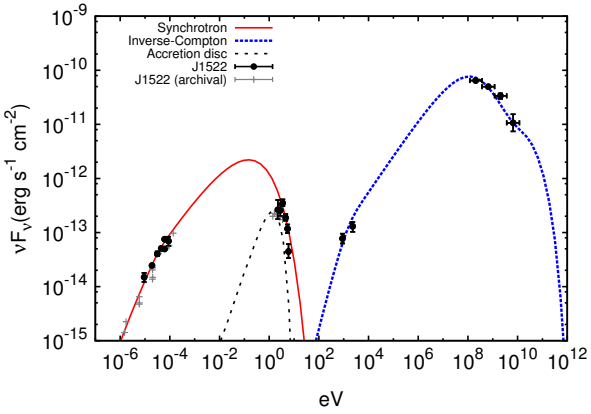
Synchrotron
Inverse-Compton
Accretion disc
J1522
J1522 (archival)
vF$_\nu$(erg s^{-1} cm^{-2})
eV

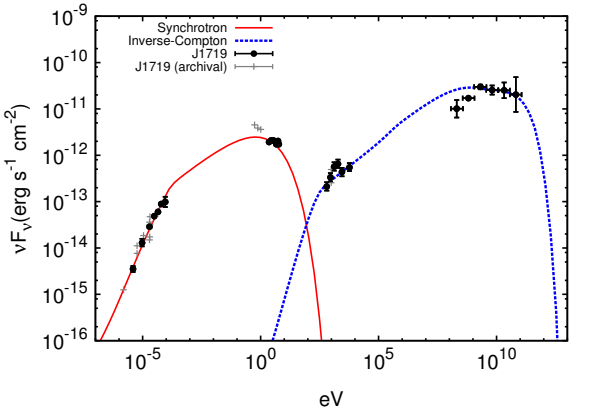
Synchrotron
Inverse-Compton
J1719
J1719 (archival)
vF$_\nu$(erg s^{-1} cm^{-2})
eV

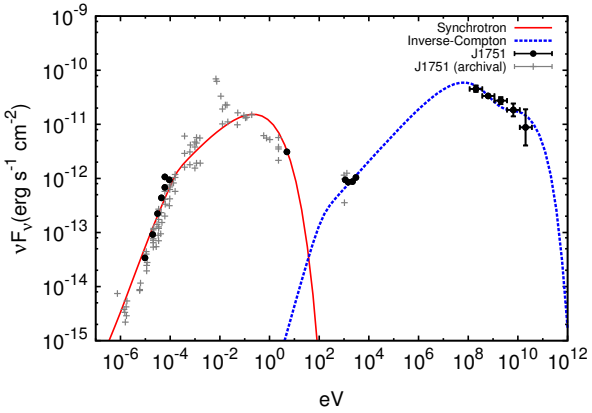
Synchrotron
Inverse-Compton
J1751
J1751 (archival)
vF$_\nu$(erg s^{-1} cm^{-2})
eV

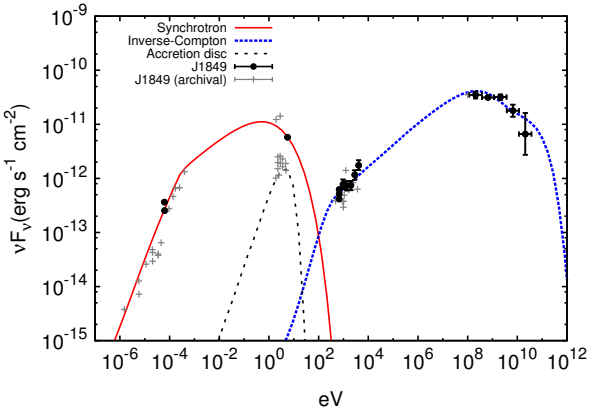
Synchrotron
Inverse-Compton
Accretion disc
J1849
J1849 (archival)
vF$_\nu$(erg s^{-1} cm^{-2})
eV

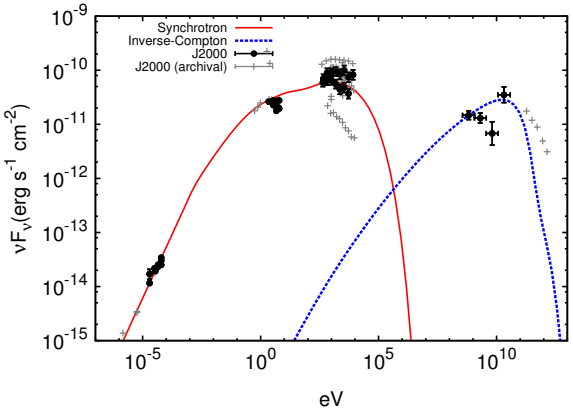
Synchrotron
Inverse-Compton
J2000
J2000 (archival)
vF$_\nu$(erg s^{-1} cm^{-2})
eV

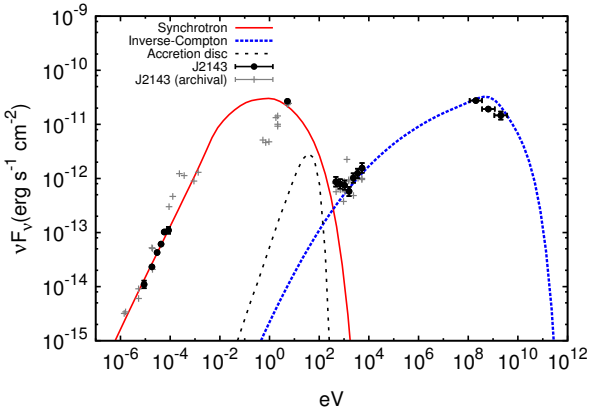
Synchrotron
Inverse-Compton
Accretion disc
J2143
J2143 (archival)
vF$_\nu$(erg s^{-1} cm^{-2})
eV

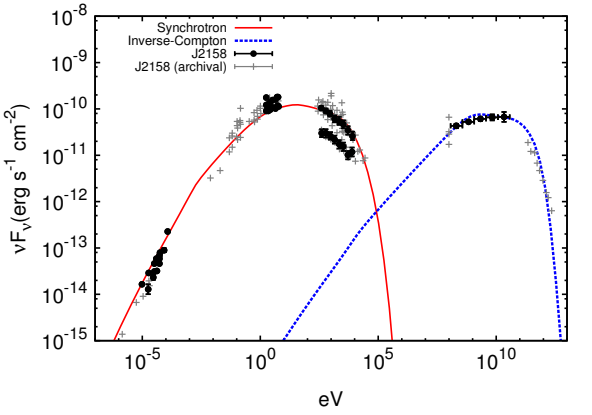
Synchrotron
Inverse-Compton
J2158
J2158 (archival)
vF$_\nu$(erg s^{-1} cm^{-2})
eV

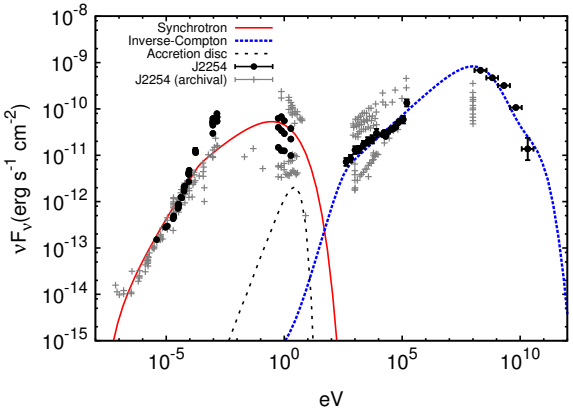
Synchrotron
Inverse-Compton
Accretion disc
J2254
J2254 (archival)
vF$_\nu$(erg s^{-1} cm^{-2})
eV

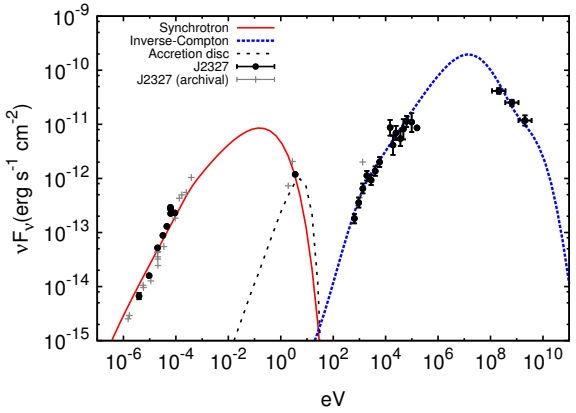
Synchrotron
Inverse-Compton
Accretion disc
J2327
J2327 (archival)
νF_ν(erg s^-1 cm^-2)
eV

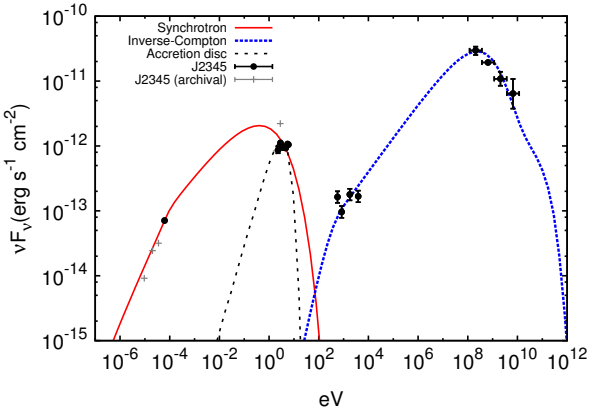
Synchrotron
Inverse-Compton
Accretion disc
J2345
J2345 (archival)
νF_ν(erg s^-1 cm^-2)
eV

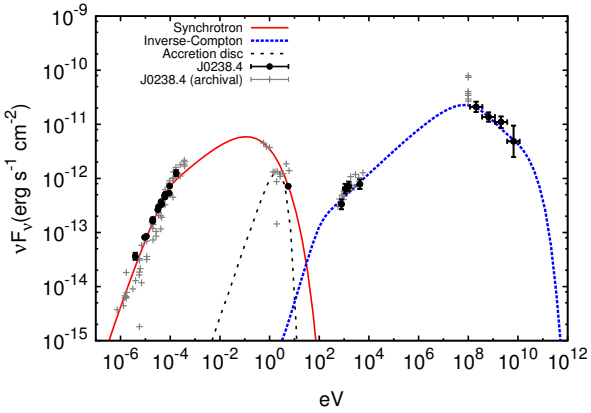
Synchrotron
Inverse-Compton
Accretion disc
J0238.4
J0238.4 (archival)
νF_ν(erg s^-1 cm^-2)
eV

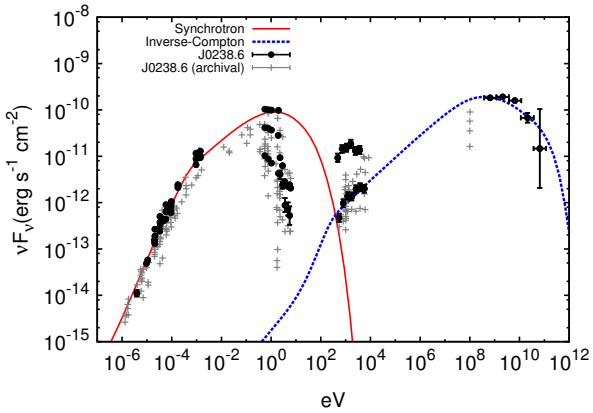
Synchrotron
Inverse-Compton
J0238.6
J0238.6 (archival)
νF_ν(erg s^-1 cm^-2)
eV

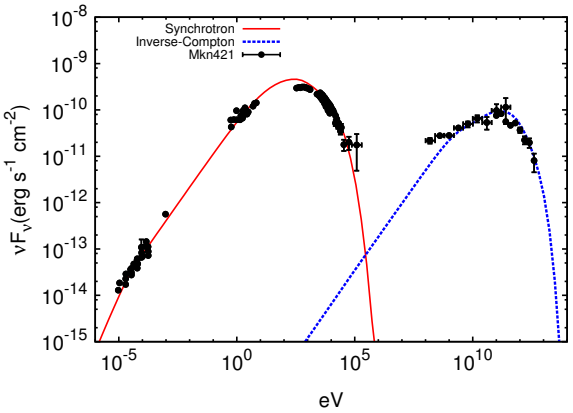
Synchrotron
Inverse-Compton
Mkn421
νF_ν(erg s^-1 cm^-2)
eV

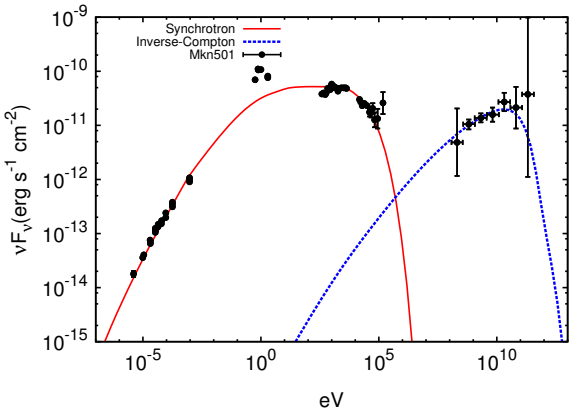
Synchrotron
Inverse-Compton
Mkn501
νF_ν(erg s^-1 cm^-2)
eV

Comparison to existing models

- Existing spherical blob and cylindrical jet emission models are successful at high frequencies but cannot reproduce the observed radio emission produced by the large scale structure of the jet.

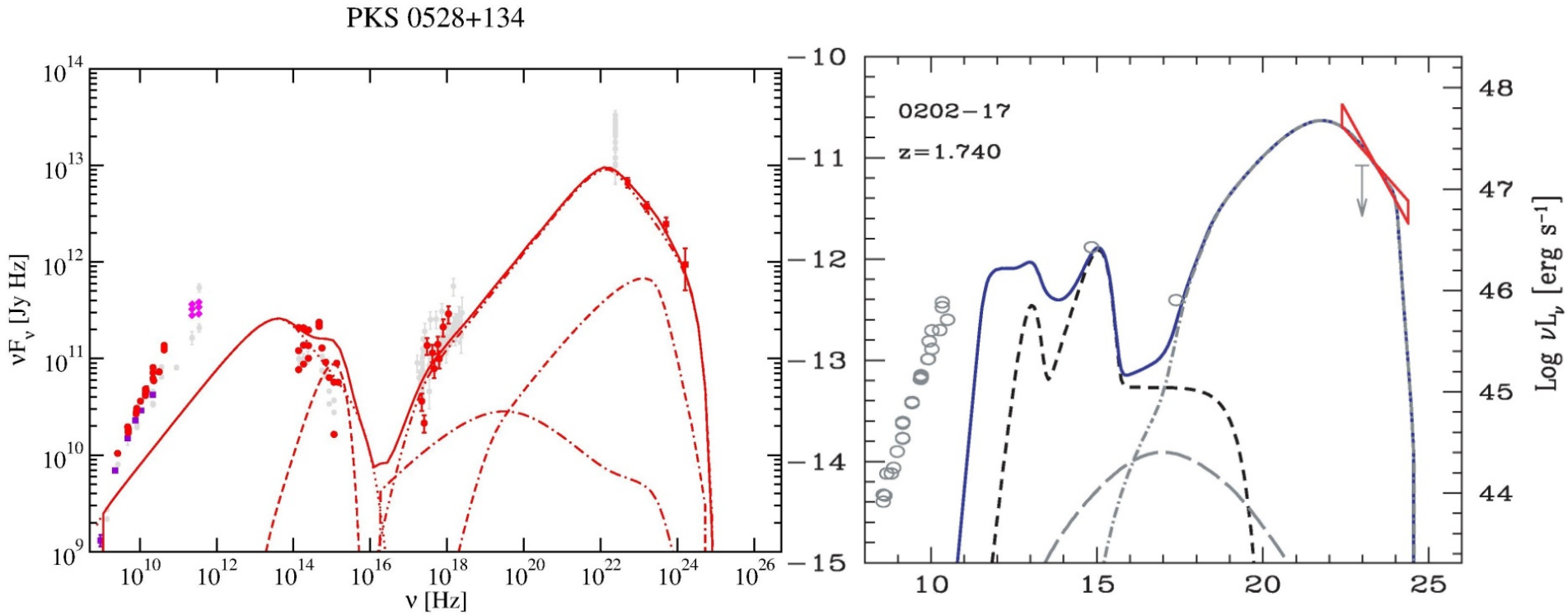

Bottcher et al. 2013

Ghisellini et al. 2009

Constraining the radius of the transition region

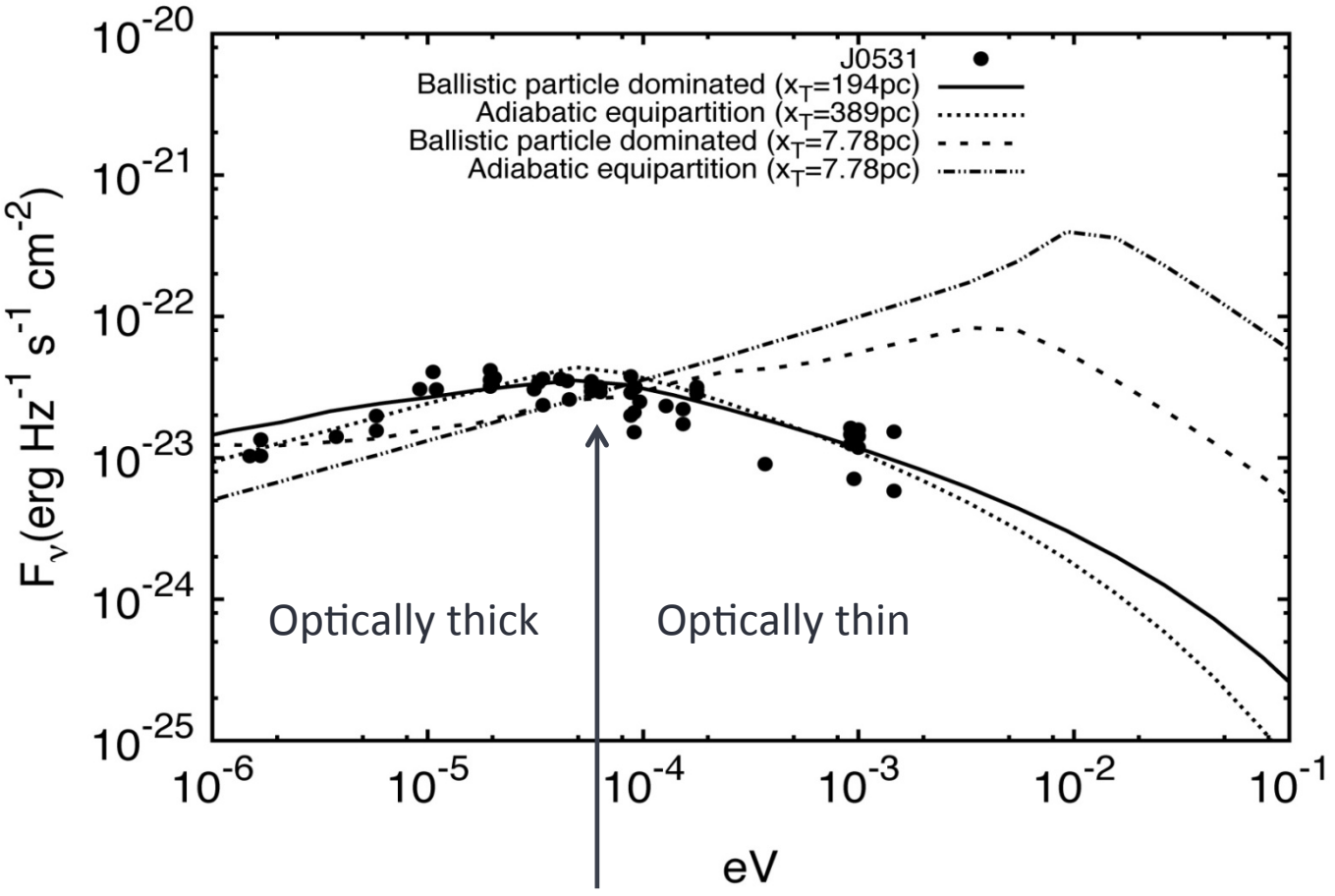

Synchrotron break

Potter and Cotter 2013b

An approximately linear relation between jet power and transition region radius!

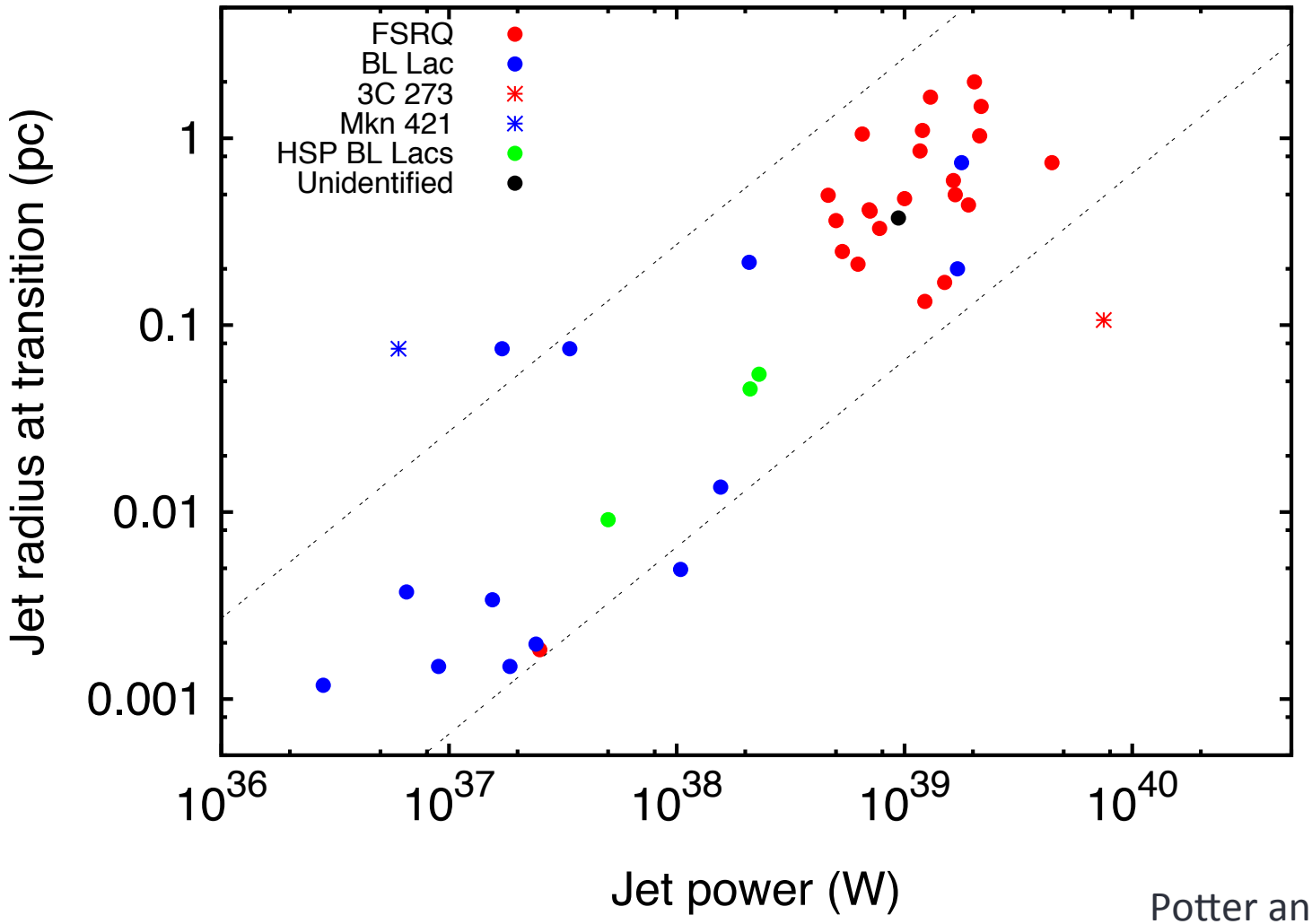

Potter and Cotter 2015

Jet power vs. bulk Lorentz factor

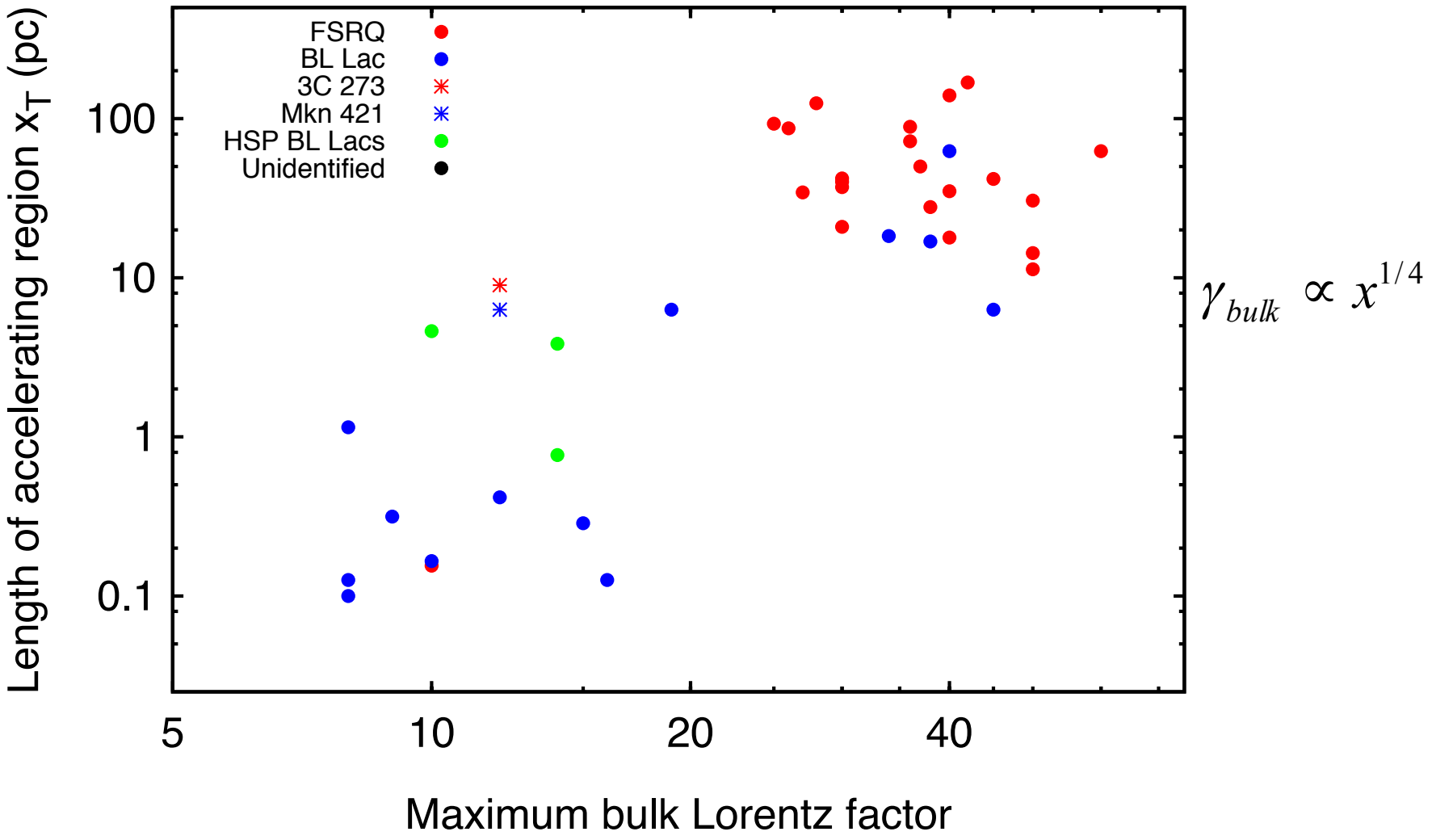

Potter and Cotter 2015

Time-dependent flares

- Using the same fluid model as before we allow the plasma properties to be time-dependent.
- The flare is described by three parameters: the distance of the flaring front at which particle acceleration occurs, the equipartition ratio of plasma leaving the flare and the effective jet power of the flaring plasma.

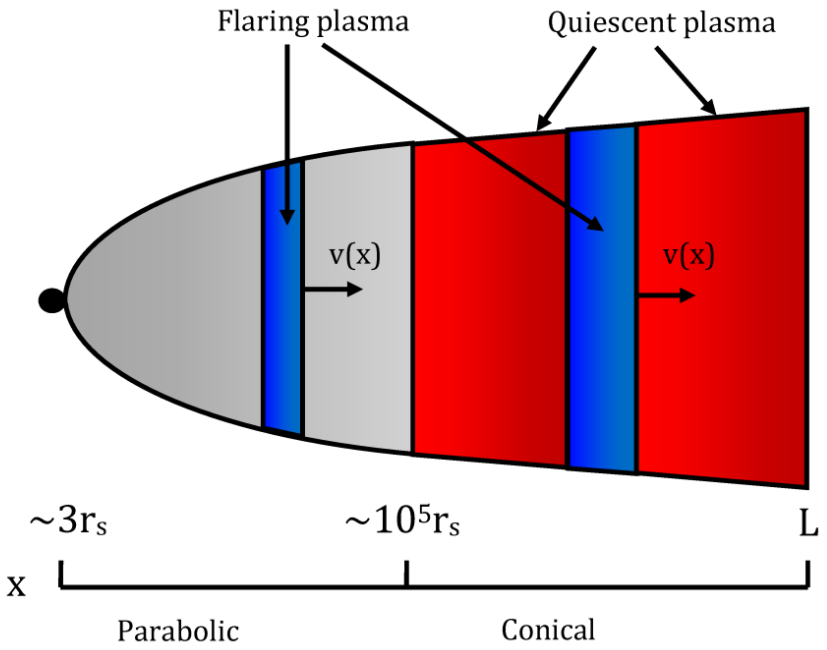

Multiwavelength flare in PKS1504

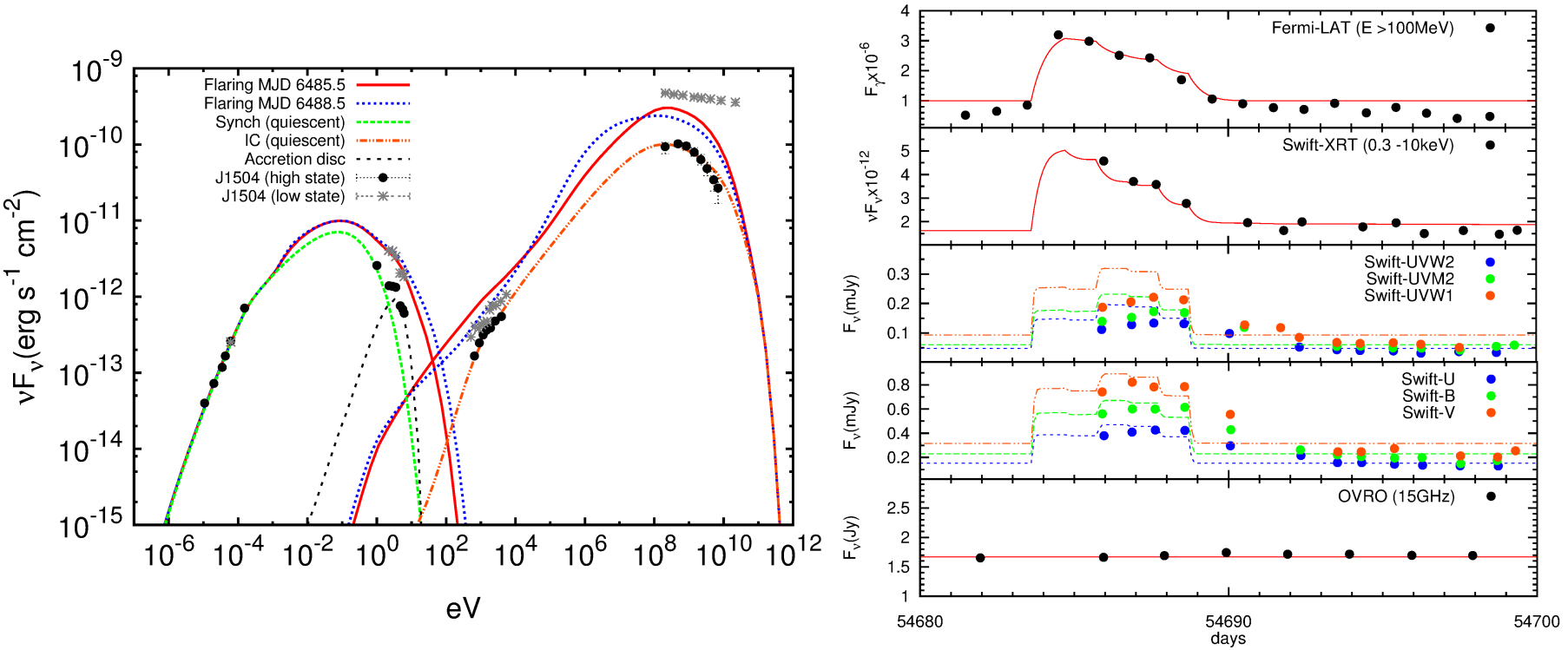

- This multiwavelength flare can be well fitted by an equipartition flare occurring in the BLR with the same parameters as the quiescent jet plasma.

Potter 2018 MNRAS

Flaring behaviour

- The rise and decay time of a flare are both approximately equal to the radiative lifetime of the emitting electrons.
- This is the timescale taken to fill and deplete the maximum volume of flaring plasma trailing the flaring front (the radiative lengthscale).
- Since the radiative lifetime of the highest energy electrons is shortest, X-ray/UV synchrotron and gamma-rays are the fastest to respond (can lead to orphan flares if a flare is short).
- Longer duration flares have time to respond to the time-dependence of the electron acceleration process.
- Radio flares act as a long-term moving average of the jet power smoothed on the radiative lifetime, and with a frequency dependent lag.

Potter 2018

Radio flare in Mkn 501

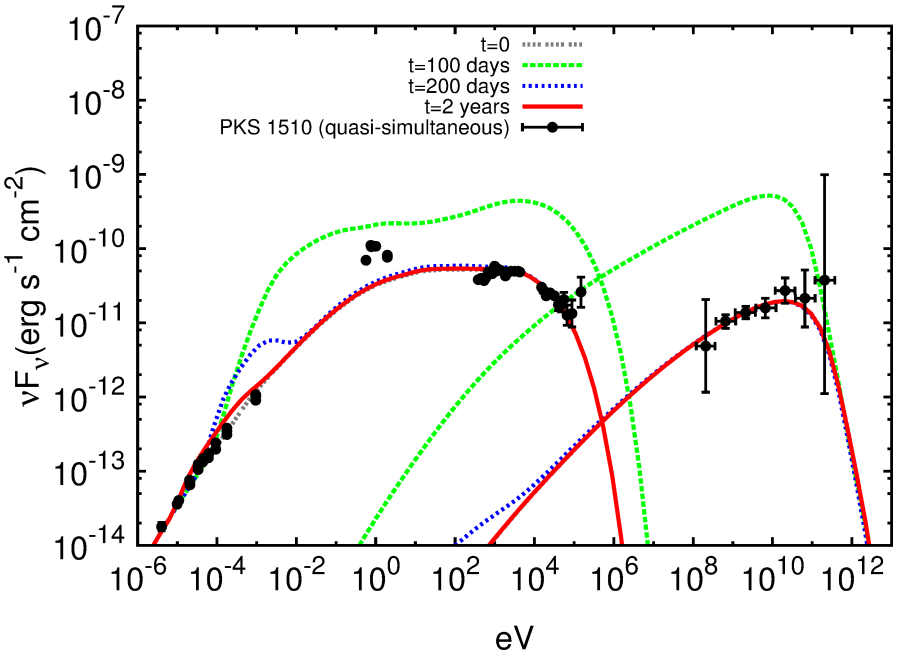

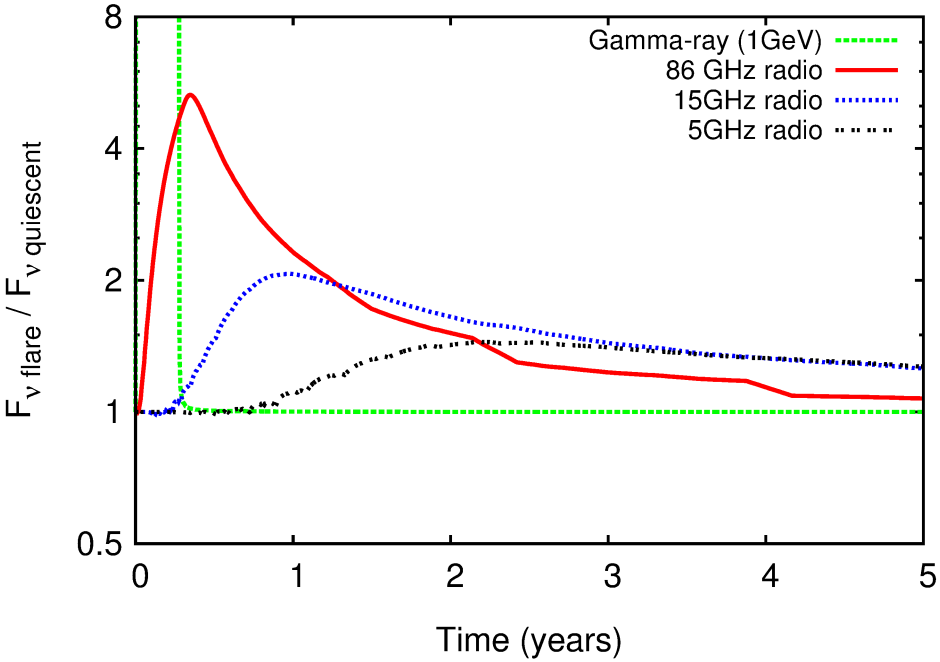

- Increasing the power of the jet in Mkn 501 by a factor of 10 for 100 days leads to an observable radio flux increase.
- The radio lag and rise time increase as frequency decreases and are ~months at 15GHz.

Potter 2018

Radio Flare in an FSRQ (PKS 1510)

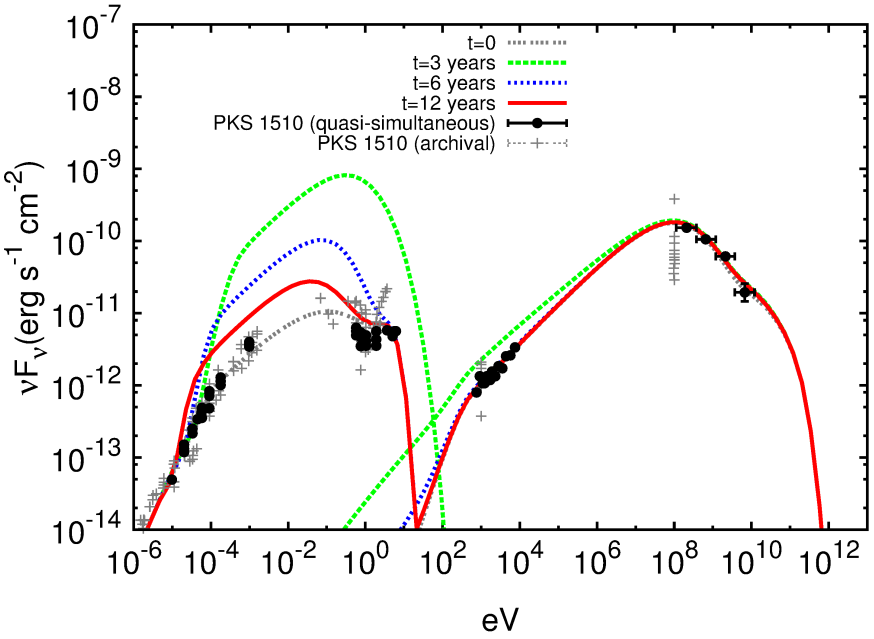

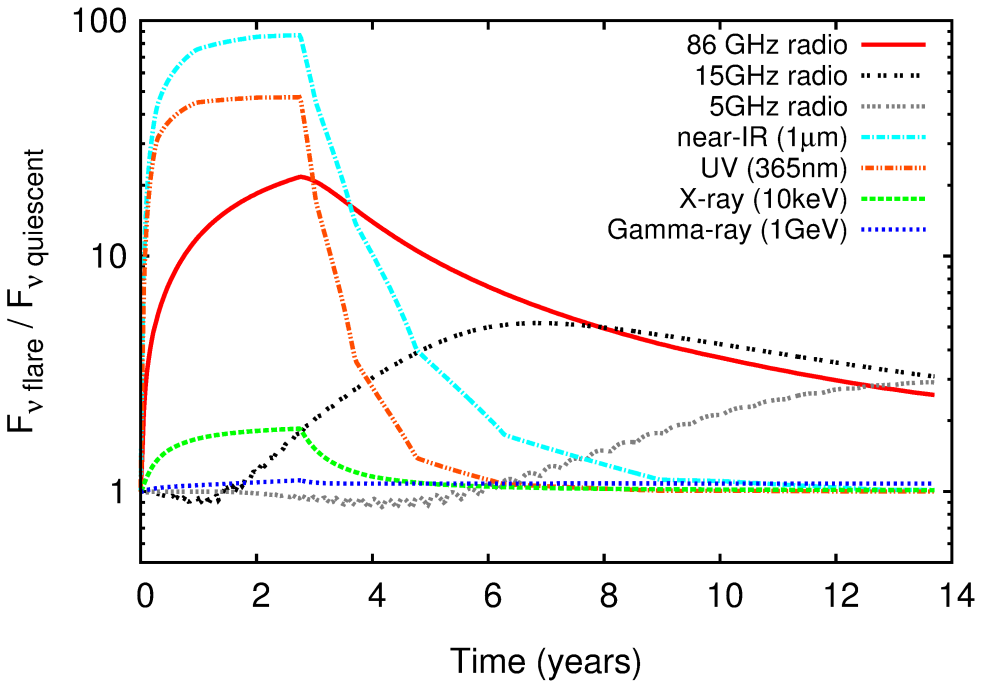

- In more powerful FSRQ jets the optically thin region is at a larger distance from the prompt high energy emission, so the radio lag and rise time are longer ~ years at 15Ghz.

Potter 2018

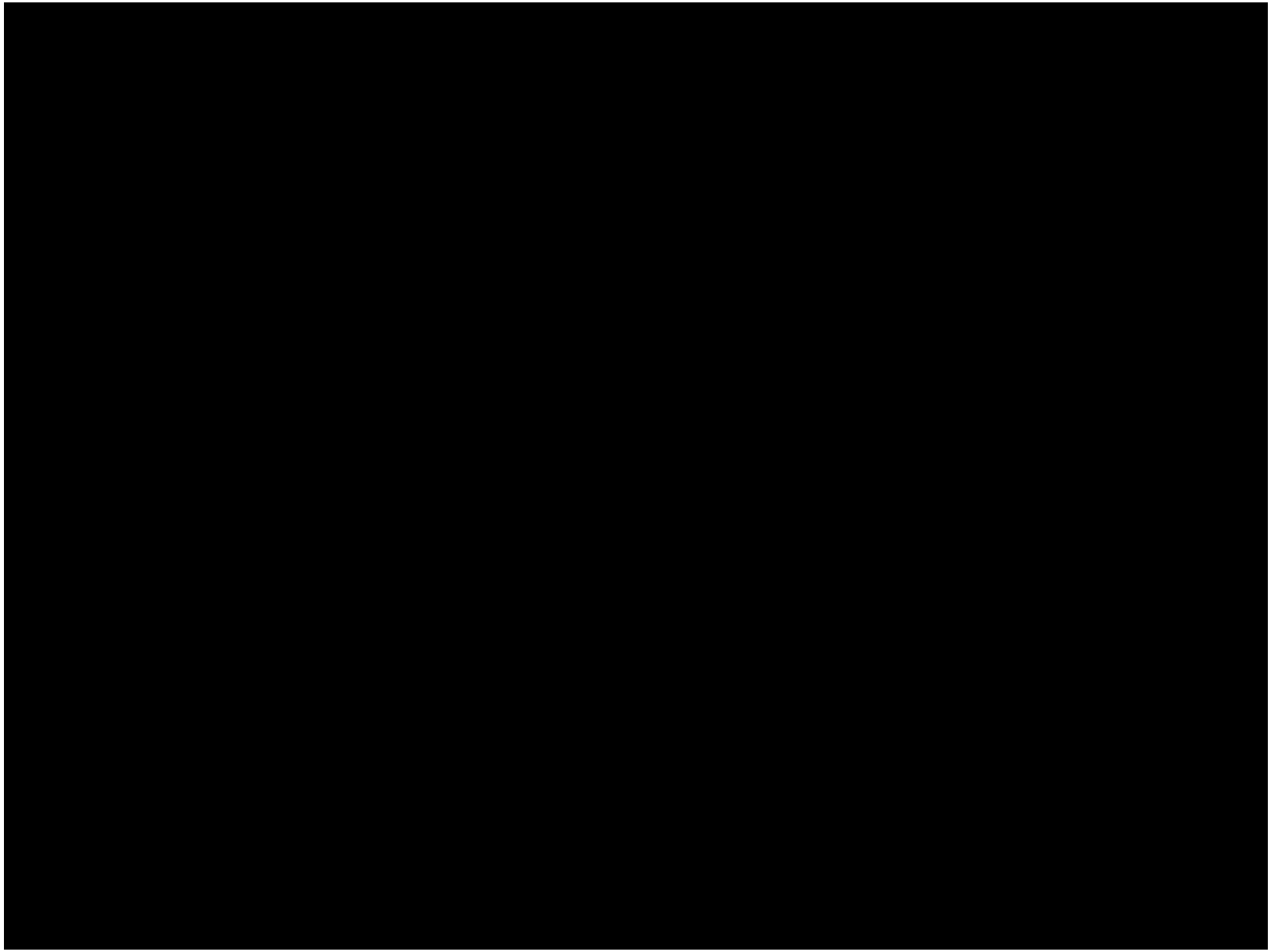

Orphan Flares

- Orphan flares occur when the timescale of the flare is shorter than the radiative lifetime at most frequencies.
- Only the most luminous high energy synchrotron or IC emission responds fast enough to be observed over the quiescent emission.

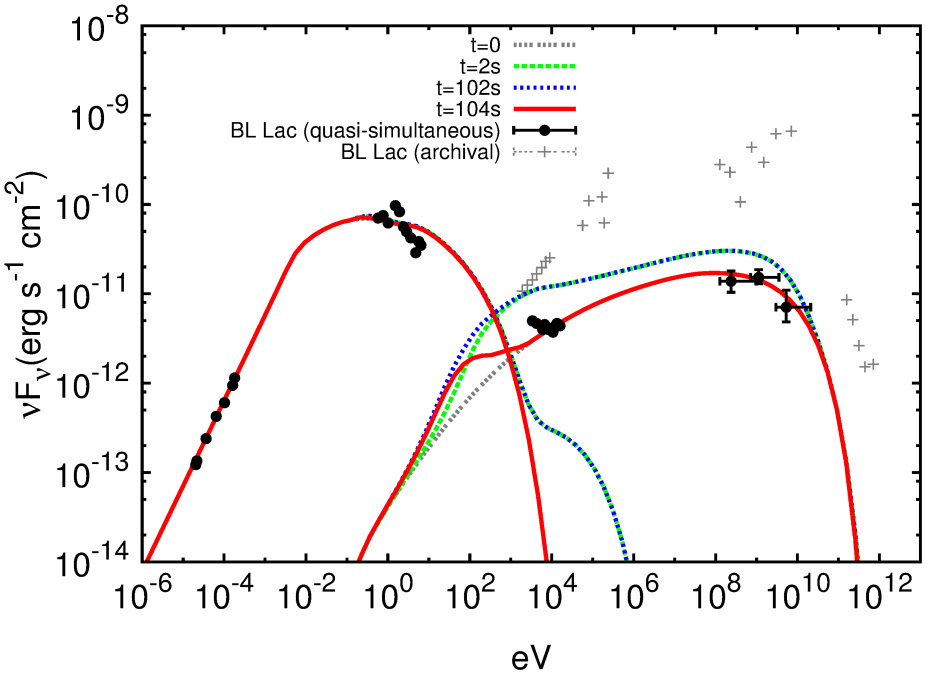

Orphan Inverse-Compton flare

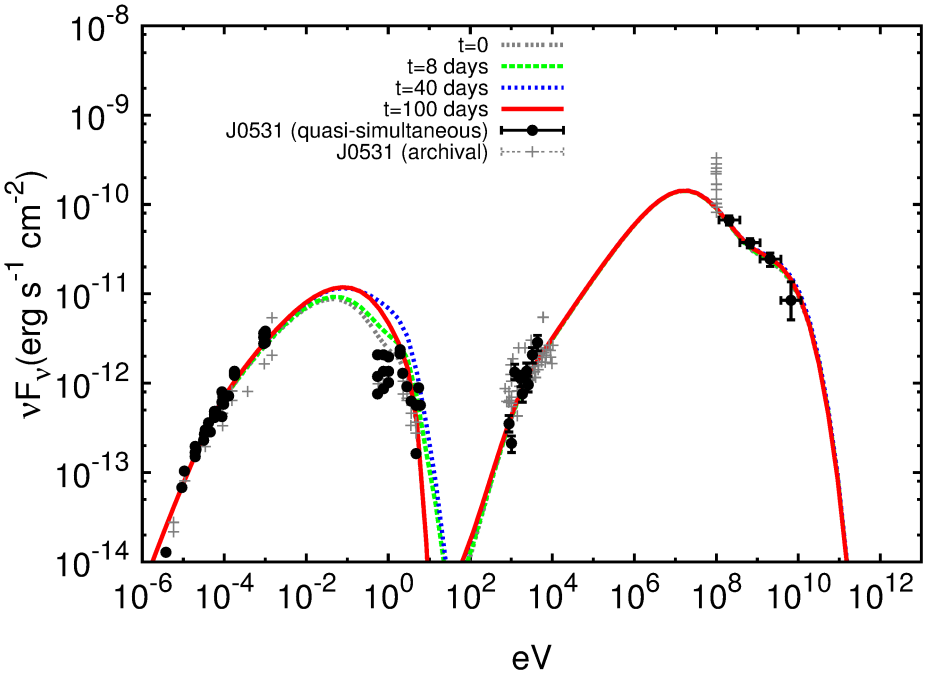

Orphan synchrotron flare

Conclusions

- Our relativistic extended fluid jet emission model is the first full spectrum blazar model.
- Modelling radio emission and the synchrotron break we find that more powerful FSRQ jets remain magnetised and accelerate for larger distances than weaker BL Lac jets.
- The intrinsic rise/decay time of a flare is determined by the radiative lifetime at a given frequency.
- We therefore expect short symmetric flares and longer structured flares.
- Radio flares reflect long-term changes in jet power.
- Radio lags and rise/decay timescales can be used to determine jet properties and increase in higher power blazars with timescales of ~months-decades.

Rise and decay timescales

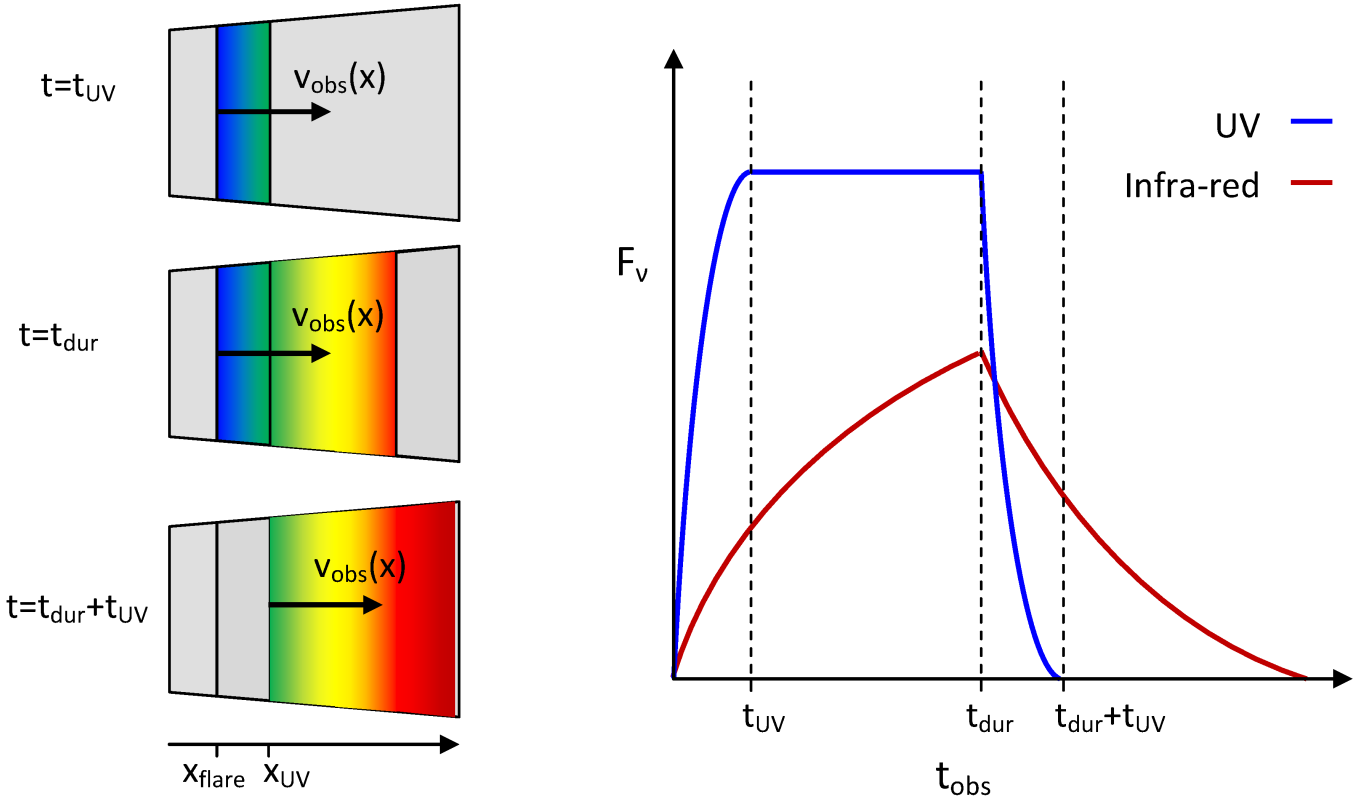

- Flaring emission rises and decays on the radiative lifetime.

Evidence for AGN unification

- Similar Eddington distribution to AGN observations of radiatively inefficient Low Excitation Radio Galaxies (FRIs) and radiatively efficient High Excitation Radio Galaxies (FRIIs).

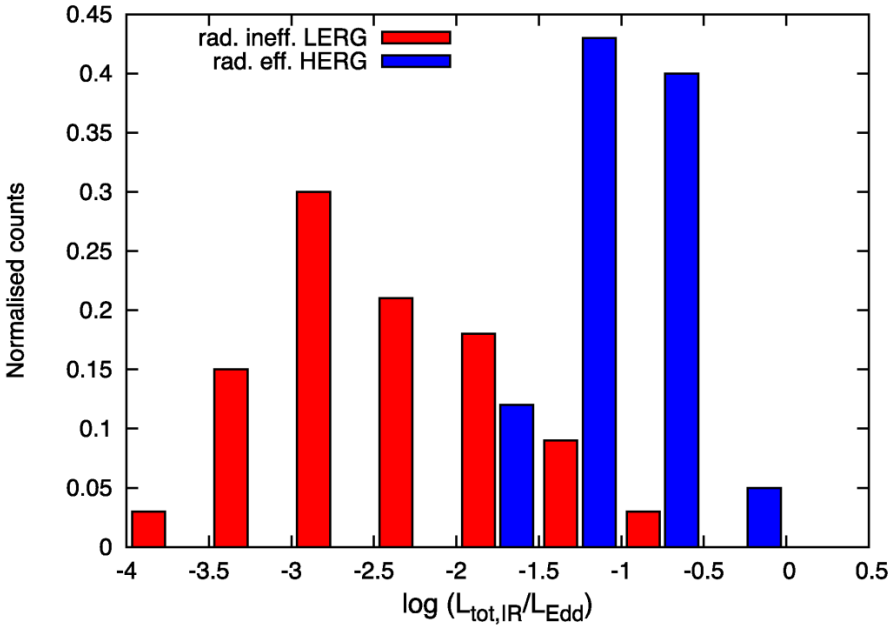

Mingo et al. 2014

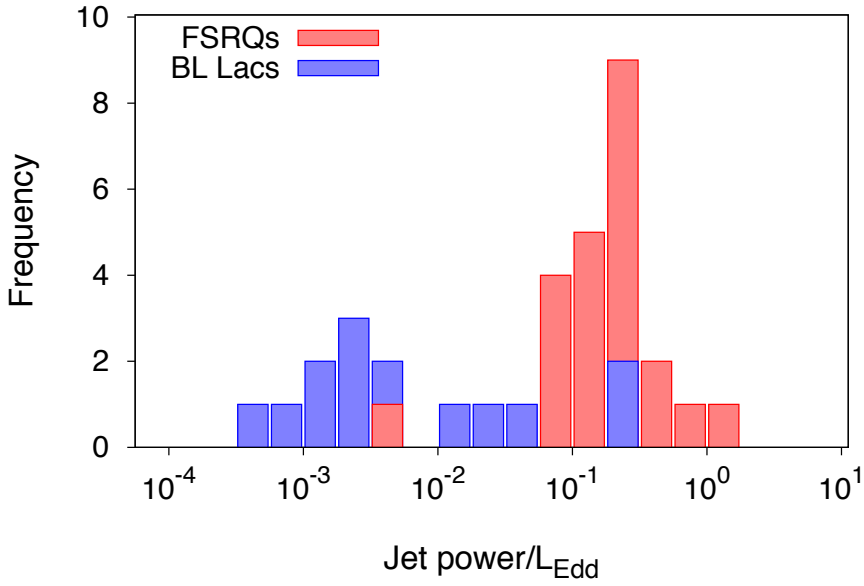

P+C 2015

Evidence for an accretion mode dichotomy

- Assuming a fiducial mass MBH=5x$10^8 M_{Sun}$ for all FSRQs and BL Lacs (Shaw et al. 2013).
- The distance in r_s at which the jet comes into equipartition is much larger in FSRQs than BL Lacs.
- The Eddington accretion rate is much lower in BL Lacs than FSRQs.

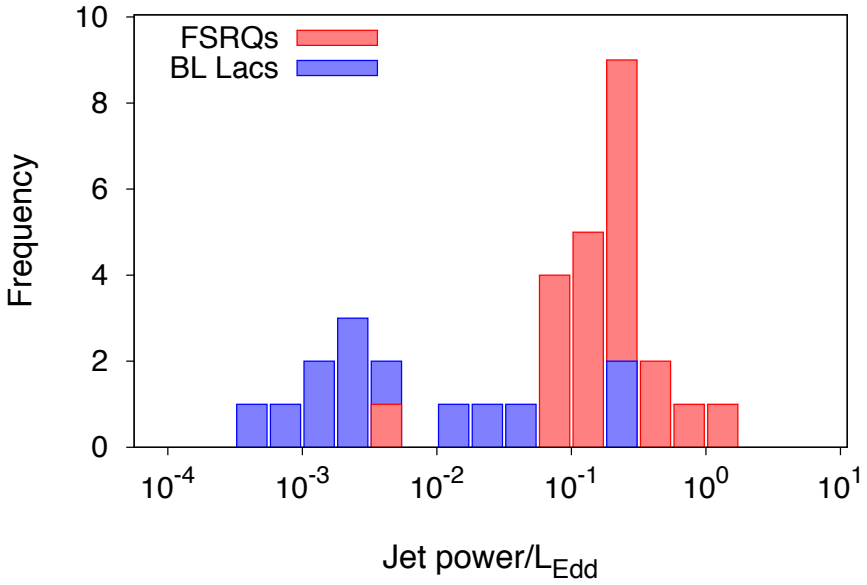

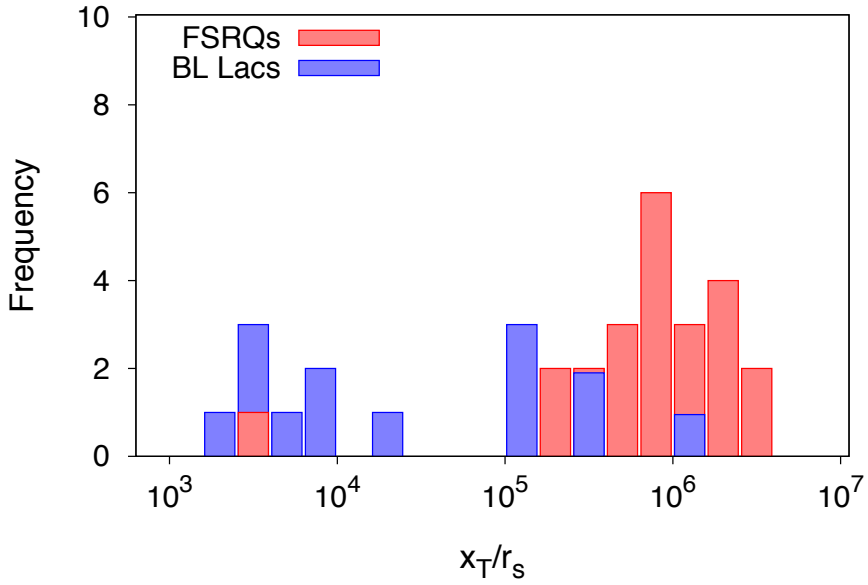

P+C 2015

Summary

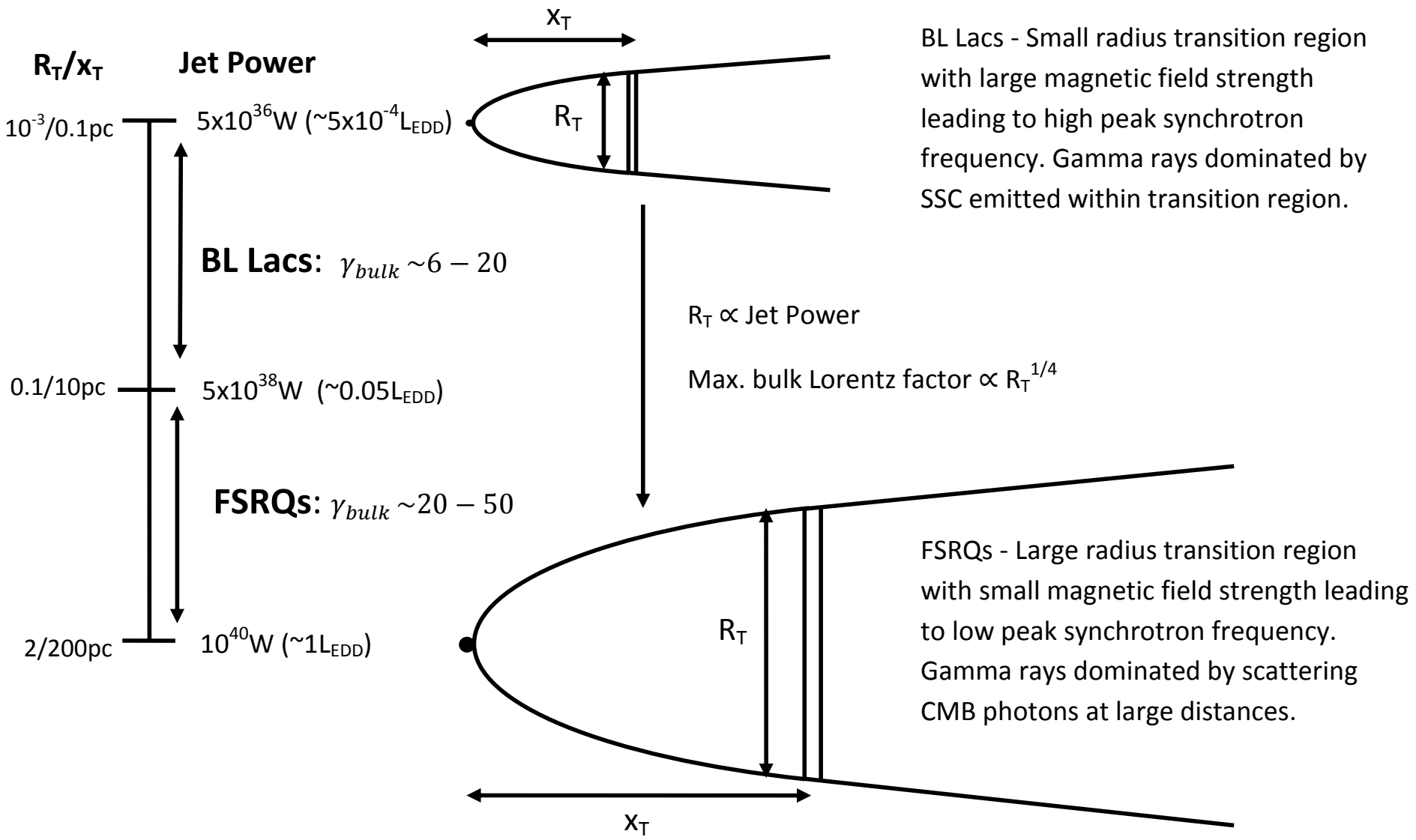

BL Lacs - Small radius transition region with large magnetic field strength leading to high peak synchrotron frequency. Gamma rays dominated by SSC emitted within transition region.

$R_T \propto$ Jet Power

Max. bulk Lorentz factor $\propto R_T^{1/4}$

FSRQs - Large radius transition region with small magnetic field strength leading to low peak synchrotron frequency. Gamma rays dominated by scattering CMB photons at large distances.

Powerful jets must be highly magnetised!

- We demand that at least 5% of the total initial energy in the plasma remains in the plasma to large distances and is not radiated away by synchrotron and synchrotron self-Compton (i.e. $f_{loss}>0.05$).
- For typical jet parameters with a fixed magnetisation we constrain high power jets ($>0.1L_{Edd}$) to be strongly magnetically dominated $U_B/U_{e\pm}>10^4$, independently of black hole mass.

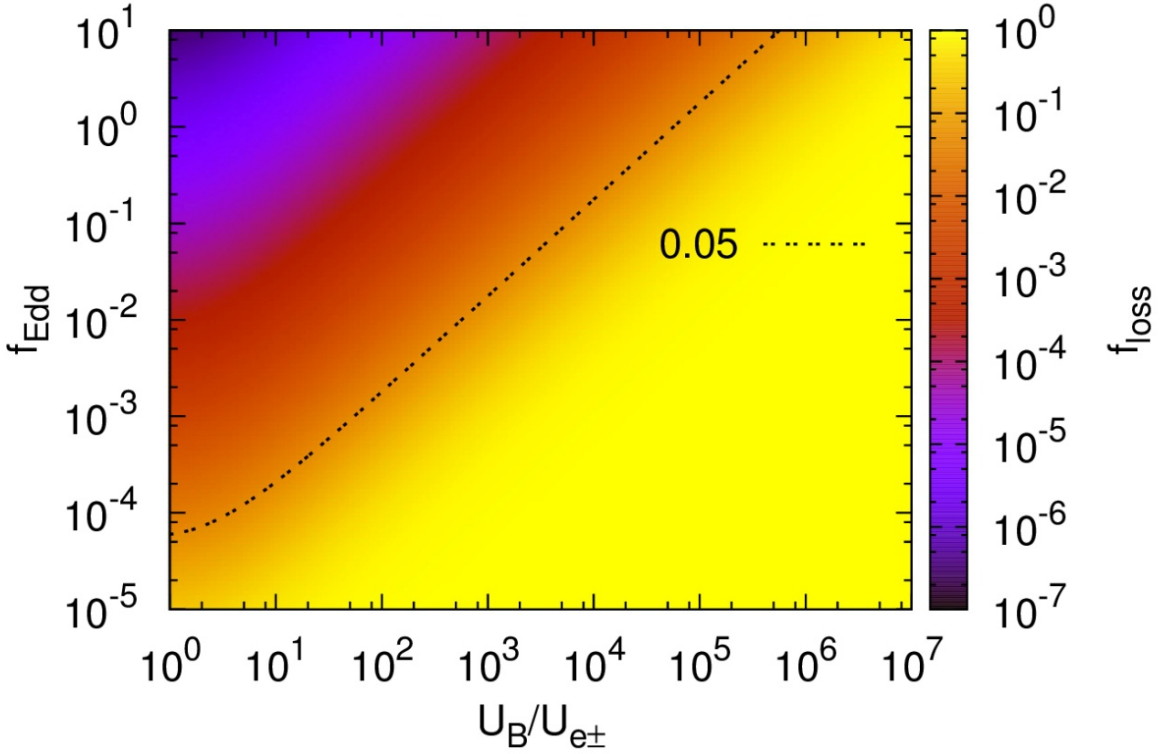

for $E_{\max} = 10^4 m_e c^2$

Potter 2016 in press

External photon fields

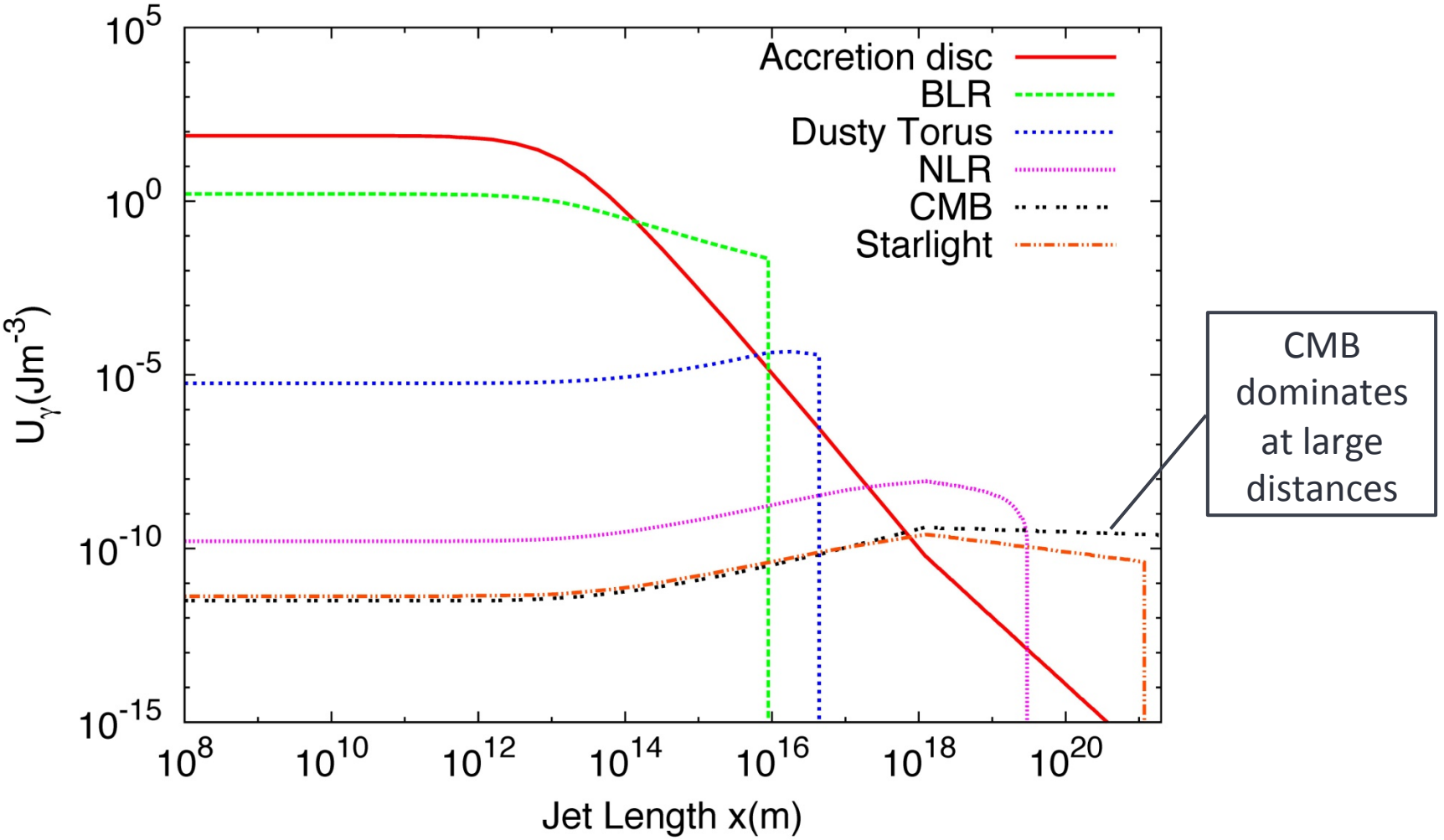

Potter and Cotter 2013a

A fluid jet model – conservation of energy

- We assume jet properties only depend on the jet length and are homogeneous perpendicular to the jet axis.
- Since we allow the jet velocity and shape to change as a function of distance conservation of relativistic energy-momentum takes the form.

$$\nabla_\mu T^{\mu\nu} = 0, \qquad T^{\mu\nu} = T^{\mu\nu}_{\text{Magnetic}} + T^{\mu\nu}_{\text{Particles}} + T^{\mu\nu}_{\text{Losses}}$$

- In order to relate plasma properties in the rest frame and lab frame we treat the plasma as a relativistic perfect fluid.

$$T'^{\mu\nu} = \begin{pmatrix} \rho' & 0 & 0 & 0 \\ 0 & \frac{\rho'}{3} & 0 & 0 \\ 0 & 0 & \frac{\rho'}{3} & 0 \\ 0 & 0 & 0 & \frac{\rho'}{3} \end{pmatrix} \qquad T^{\mu\nu}(x) = \Lambda^{\mu}_{\ a} T'^{ab} \Lambda^{\nu}_{\ b} = \begin{pmatrix} \frac{4}{3}\gamma_{\text{bulk}}(x)^2\rho' & \frac{4}{3}\gamma_{\text{bulk}}(x)^2\rho' & 0 & 0 \\ \frac{4}{3}\gamma_{\text{bulk}}(x)^2\rho' & \frac{4}{3}\gamma_{\text{bulk}}(x)^2\rho' & 0 & 0 \\ 0 & 0 & \frac{\rho'}{3} & 0 \\ 0 & 0 & 0 & \frac{\rho'}{3} \end{pmatrix}$$

- Integrating conservation of energy over the jet volume and using the divergence theorem we find the conservation of energy equation for the jet.

$$\int \nabla_\mu T^{\mu\nu} \mathrm{d}^4 V = \int T^{\mu\nu} \mathrm{d}^3 S^\mu = \frac{\partial}{\partial x}\left(\frac{4}{3}\gamma_{\text{bulk}}(x)^2 \pi R^2(x)\rho'(x)\right) = 0$$